Radial Compensation: Stable and Semantically Decoupled Generative Models on Riemannian Manifolds

Marios Papamichalis*

Regina Ruane[†]

Abstract

Generative models on curved spaces hinge on the chart that links Euclidean backbones to the manifold. Exponential maps preserve geodesics but have stiff, radius-dependent Jacobians, while volume-preserving charts keep densities well conditioned but warp geodesic distances. Both choices entangle curvature with model parameters and inflate gradient variance, and in high-dimensional latent continuous normalising flows on CIFAR-10 the usual wrapped exponential prior can drive radii far beyond the curvature scale, causing test likelihoods to deteriorate and ODE solvers to become extremely stiff. We introduce Radial Compensation (RC), an information–geometric recipe for choosing the base density in the tangent space so that, after any scalar-Jacobian azimuthal chart, the likelihood on the manifold depends on samples only through their geodesic distance from a pole, and that geodesic radius matches a chosen one-dimensional Euclidean radial model with the same Fisher information. This decouples parameter semantics from curvature: radial parameters keep their usual meaning in geodesic units, while the chart can be tuned purely as a numerical preconditioner. We prove a balanced polar pushforward theorem that extends RC to manifolds with known geodesic polar volume, and show that, within isotropic bases and scalar-Jacobian (spherically symmetric) azimuthal charts, RC is essentially the only construction that yields geodesic-radial likelihoods with chart- and curvature-invariant Fisher information. Within this regime we derive the Balanced-Exponential (bExp) family of charts, a one-parameter family interpolating between equal-area Lambert and the exponential map that uniquely minimises a convex trade-off between volume distortion and geodesic error. Under RC, all settings of the bExp dial realise the same manifold density and Fisher information, while smaller dial values provably reduce chart-induced gradient variance and continuous-flow cost. Empirically, RC yields semantically decoupled, stable generative models across synthetic densities, hyperspherical and mixed-curvature VAEs, latent continuous flows on image benchmarks, hyperbolic flows on graphs, and protein orientation models. RC restores parameter-clean geodesic radii, makes curvature a meaningful and interpretable hyperparameter, and either matches or improves likelihood at fixed architecture and training budget. In particular, RC-bExp prevents the catastrophic radius blow-ups observed with standard charts in high-dimensional latent flows and improves evidence lower bounds and curvature interpretability in mixed-curvature VAEs, making RC-bExp a robust default for likelihood-trained generative models on manifolds.

1 Introduction

Modern generative models on curved spaces, most notably spheres \mathbb{S}^n and hyperbolic spaces \mathbb{H}^n , increasingly underpin representation learning for directional data, hierarchical structure, and geometry-aware latent variables. A large body of work keeps a Euclidean backbone (VAE, flow, CNF) and wraps it through geometry-aware charts to obtain manifold densities: early Riemannian flows on submanifolds and spheres use homeomorphisms and stereographic/exponential mappings [11], later extended to Lie groups [9], to tori and spheres with invertible spherical/toric layers [16], and to hyperbolic spaces with coupling architectures [2]. Mixed-Curvature VAEs place latents in products of constant-curvature components with Wrapped Normal priors and (optionally) learnable curvature parameters [18]. Hyperspherical VAEs instead use von Mises-Fisher (vMF) priors and posteriors on the unit sphere [5, 6]; Hyperbolic VQ-VAEs endow the VQ-VAE codebook with a Poincaré-ball prior and report that performance is remarkably insensitive to the exact curvature value

^{*}Human Nature Lab, Yale University, New Haven, CT 06511, marios.papamichalis@yale.edu

[†]Department of Statistics and Data Science, The Wharton School, University of Pennsylvania, 3733 Spruce Street, Philadelphia, PA 19104-6340, ruanej@wharton.upenn.edu

[4]. In parallel, probabilistic primitives on curved spaces have been developed—including hyperspherical posteriors for VAEs [6], the hyperbolic wrapped normal [14], and wrapped families on homogeneous manifolds [10]. Normalizing flows in Euclidean space are by now well surveyed [15], and many of these constructions carry over to curved spaces via suitable charts.

Alongside these wrapped / coordinate-based models, a complementary line of work defines flows intrinsically on manifolds. Riemannian continuous normalizing flows parametrize vector fields and solve ODEs directly on the manifold [13, 12, 8], while divergence- or path-based training circumvents per-iteration ODE solves via Moser flows [17] or probability-path divergences [1]. Diffusion/score-based and flow-matching formulations have been generalized to Riemannian geometries and arbitrary manifolds, providing geometry-consistent forward processes and pathwise objectives [7, 3]. These intrinsic approaches elegantly avoid explicit coordinates, but in practice many systems still rely on Euclidean backbones plugged into chart maps because they integrate cleanly with existing flow, VAE, and CNF libraries.

Intrinsic Riemannian flows and diffusion models elegantly avoid explicit coordinates, but they also treat the manifold as a homogeneous continuum: radial distance and angular direction are updated by the same vector field, often with expensive projections and retractions at each step. In many applications, however, radius and direction carry fundamentally different semantics — "how far from the prototype" vs. "which object or subtree" in hierarchical embeddings, or "uncertainty" vs. "content" in generative latents. Chart—based models are attractive precisely because they expose this radial/angular structure to standard Euclidean backbones. Our goal is not to patch an incorrect formalism, but to characterise the unique way in which such chart—based models can remain both numerically stable and semantically faithful to the underlying manifold geometry.

Despite these intrinsic alternatives, charts are hard to avoid in practice. They provide a thin interface between existing Euclidean codebases and curved latents, let us reuse off-the-shelf coupling/ResNet blocks and CNF solvers, and are natural whenever only some layers or latent components live on manifolds (e.g., mixed-curvature VAEs, SE(3)-style orientation heads, graph embeddings) [18, 4]. In this chart-based regime, the chart is not cosmetic: it controls both numerical conditioning and how curvature enters the model parameters. Yet chart-based models are notoriously finicky. The same VAE or CNF backbone can behave well on one curvature or chart and become unstable or hard to tune on another: wrapped Gaussians drift away from their intended scale, continuous flows require tiny ODE steps, and curvature hyperparameters often appear to "not matter"—even though geometry should [18, 2, 4]. This suggests that usual chart choices force models to spend capacity and gradient signal correcting for hidden geometric artefacts rather than learning the data distribution.

The chart dilemma: curvature vs. semantics. In the chart-based regime, practitioners face a simple but consequential question: which coordinates should we use? Two canonical choices expose a fundamental incompatibility. The Riemannian exponential map preserves geodesics but injects a highly variable radial Jacobian; its polar factor $(s_{\kappa}(R)/R)^{n-1}$ amplifies curvature effects, inflates gradient variance, and makes continuous flows stiff. Equal-area azimuthal projections (Lambert maps) tame the Jacobian and are appealing for "Lambert-lift" constructions on spheres and hyperbolic spaces, but they warp geodesic radii and require atlases near cut loci [19]. In both cases, curvature couples to model parameters through the Jacobian, so that simple Euclidean radial families (Gaussians, Gammas, Weibulls, lognormals) become opaque "wrapped" laws whose effective shape and scale depend on curvature, dimension, and chart. Our results show that this is not just an implementation nuisance but a structural barrier: within a natural modelling class, any non–RC choice must break at least one of geodesic-radial likelihoods, isotropy, or Fisher-invariant radial semantics [18, 2, 4].

A motivating failure mode in practice. The abstract description above hides a very concrete pathology that arises even in otherwise standard models. Consider a high–dimensional latent continuous normalizing flow (CNF) on CIFAR–10 with a hyperbolic latent space and a wrapped Gaussian prior implemented via the raw exponential chart. The Euclidean backbone, architecture, and optimiser are all well behaved, yet during training the latent geodesic radii R = d(p, q) drift far beyond the curvature scale R_c : mass is pushed

deep into the tails where the polar factor $(s_{\kappa}(R)/R)^{n-1}$ dominates. Gradients through the chart Jacobian blow up, the instantaneous change–of–variables term becomes extremely stiff, the number of ODE function evaluations (NFEs) explodes, and test NLL deteriorates sharply. The only difference between this unstable regime and a well–behaved one is the particular choice of "wrapped prior + chart". In the same architecture, replacing the raw exponential prior by a radially compensated one stabilises the radii, restores test NLL, and cuts NFEs, without touching the CNF backbone (see Sec. 5). This vignette is representative: across VAEs, CNFs, and flows, we observe models that fail or become fragile purely because of the charted prior, even though the backbone is unchanged. RC is designed to make this kind of failure much harder to trigger.

Our main insight. The instability of chart–based models is not due to curvature alone, but to a mismatch between (i) the volume distortion of the chart and (ii) the statistics we ask the radial parameters to control. If we insist that a one–dimensional parameter θ has the same Fisher information and the same geodesic–radius law on every manifold and every chart, then there is essentially *one* compatible choice for the tangent–space base: Radial Compensation. This perspective turns chart design from an ad-hoc implementation choice into an information–geometric constraint.

Our viewpoint: fix the chart—base pair, not the manifold. We take the chart as given and repair the *pair* of chart and tangent-space base. For most applications, the desired radial semantics are simple: practitioners want to choose a one-dimensional law for the geodesic radius ("cap size", "prior scale", "margin") and have that law mean the same thing regardless of curvature or chart. This leads to a concrete question:

Can we choose the tangent-space base so that, after any reasonable scalar-Jacobian chart, the manifold density depends on a point only through its geodesic distance, and the radial parameters see exactly the same statistics as in a one-dimensional Euclidean model?

We show that the answer is yes, via $Radial\ Compensation\ (RC)$. Given any target radial density on $[0,R_{\rm max})$, RC multiplies it in the tangent space by the chart's scalar Jacobian so that, after pushforward, the geodesic radius has exactly the chosen distribution and Fisher information. Intuitively, RC takes the geometric complexity hit in the tangent space so that on the manifold "mean stays mean; variance stays variance" in geodesic units. The resulting models are geodesic-radial (likelihood depends only on distance to a pole) and, within isotropic bases and scalar-Jacobian azimuthal charts, have chart- and curvature-invariant Fisher information in the radial parameters. A balanced polar pushforward theorem extends the same construction beyond constant curvature to any manifold with known polar volume element, making RC a general recipe rather than a sphere-/hyperbolic-specific trick. The RC construction is orthogonal to modelling choices such as Wrapped Normal vs. vMF vs. Riemannian Normal families [11, 6, 14, 10] and to the choice between mixed-curvature latents and Euclidean ones [18, 4].

From an information-geometric viewpoint, RC makes the radial parameter θ live on a flat Fisher manifold that is independent of curvature and chart: the Fisher information in θ matches its one-dimensional Euclidean counterpart, the pole location is Fisher-orthogonal to θ , and the maximum-likelihood estimator of θ has the same asymptotic covariance as in Euclidean radial models. This gives clean statistical semantics in geodesic units and helps explain the optimisation and stability gains we observe in practice.

Charts as numerical preconditioners: Balanced–Exponential and GCL. Once RC has factored out the geometric volume element, different scalar-Jacobian charts induce the *same* geodesic-radial likelihood and Fisher information. This allows us to treat the chart purely as a numerical preconditioner and design it with optimisation and ODE stiffness in mind. We first characterise the complete class of such azimuthal charts: every scalar-Jacobian azimuthal chart is a Lambert lift, i.e., a Lambert equal-area map composed with a radial profile. Within this class we introduce the *Balanced–Exponential* (bExp) charts, a one-parameter family indexed by $\alpha \in [0,1]$ that interpolates between Lambert-type equal-area profiles ($\alpha = 0$) and the exponential map ($\alpha = 1$). Each bExp $_{\alpha}$ chart has a closed-form integral radial profile, is a smooth diffeomorphism on its natural domain, and has a scalar log-determinant with radial factor $(s_{\kappa}(r)/r)^{(n-1)\alpha}$. We show that bExp charts uniquely minimise a strictly convex functional that balances volume distortion against geodesic error, so the dial α parametrises the lower Pareto frontier of this trade-off. Under RC, changing α leaves the

manifold density and base Fisher information invariant, while provably shrinking chart-induced gradient variance as $O(\alpha^2)$ and reducing continuous-flow NFEs roughly as $O(1/\alpha)$.

For applications where exact geodesics are non-negotiable (e.g., geodesic caps, margins, or hierarchical depths), we also construct a $Geodesic-Corrected\ Lambert\ (GCL)$ chart. GCL restores exact geodesic radii within the Lambert toolkit while retaining a scalar, radius-only Jacobian. We prove that no azimuthal chart on a curved manifold can be both volume- and geodesic-preserving, characterise the unavoidable near-cut-locus blow-up, and design a simple two-chart atlas on spheres with smooth gating that avoids cut loci while keeping log-likelihoods globally C^1 (and, under mild conditions, C^2) with bounded gradients.

Empirical behaviour at a glance. We evaluate RC and our charts across flows, VAEs, CNFs, and graph/feature models on spheres, hyperbolic spaces, and simple non-constant-curvature manifolds. On synthetic densities in \mathbb{S}^2 and \mathbb{H}^2 , RC combined with Exp/bExp/GCL exactly recovers the intended geodesic-radial families (Normal, Gamma, Weibull, lognormal), while the raw exponential chart systematically mis-calibrates shape and scale due to the curvature factor. In hyperspherical VAEs on MNIST, replacing wrapped Gaussians by RC latents improves test NLL and yields posterior radii that better match their intended one-dimensional priors. In mixed-curvature VAEs, RC-bExp improves ELBO on MNIST by about 7 nats relative to the wrapped-Exp baseline, primarily by reducing the KL term, and drives the learned curvatures toward interpretable values (flattening the spherical factor and sharpening the hyperbolic one). In latent CNFs on CIFAR-10, RC-bExp leaves test likelihood essentially unchanged while the bExp dial produces the predicted variance and stiffness scaling (chart-term variance $\propto \alpha^2$, NFEs $\propto 1/\alpha$); naïve Exp charts, in contrast, can push mass to extreme radii and severely deteriorate test NLL. Across hyperbolic flows on WordNet, \mathbb{S}^3 protein orientation models, and hyperbolic graph embeddings, RC upgrades match or improve likelihood at essentially unchanged solver cost while improving geodesic calibration and keeping radial semantics stable across curvatures.

Contributions. In summary, our contributions are:

- RC as the essentially unique Euclidean \leftrightarrow manifold adapter. We formalise Radial Compensation as a balanced polar pushforward that turns any one-dimensional Euclidean radial family into a geodesic-radial manifold model whose likelihood, Fisher information, and KL in the radial parameters match their Euclidean counterparts. On constant-curvature spaces we prove that, within isotropic bases and scalar–Jacobian (spherically symmetric) azimuthal charts, RC is essentially the only construction that achieves chart– and curvature–invariant radial semantics (Theorem 4, Corollary 1). Any non–RC choice in this dominant modelling class must break at least one of geodesic–radial likelihoods, isotropy, or Fisher–invariant radial parameters.
- Balanced charts as numerical preconditioners: bExp and GCL. Once RC factors out the geometric volume element, the chart can be treated purely as a numerical preconditioner. We show that every scalar–Jacobian azimuthal chart is a Lambert lift of a 1D radial profile and derive the Balanced–Exponential (bExp) family as the unique minimiser of a strictly convex functional balancing volume distortion against geodesic error (Theorem 7). Its dial α parametrises the lower Pareto frontier between geodesic fidelity and Jacobian regularity, while leaving the underlying manifold density unchanged under RC. In parallel, we construct a Geodesic–Corrected Lambert (GCL) chart with exact geodesic radii and scalar Jacobian, prove a "no free lunch" result showing that no azimuthal chart can be both volume—and geodesic—preserving, and design a simple two–chart atlas on spheres with globally well–behaved objectives.
- Information—geometric and optimisation consequences. We show that RC induces a flat Fisher geometry in the radial parameters: the Fisher information in these parameters matches its one–dimensional Euclidean counterpart, the pole location is Fisher–orthogonal, and Fisher–efficient learning rates are independent of curvature and chart (Corollary 2). Within this RC regime we prove that the bExp dial leaves the likelihood invariant but shrinks chart–induced gradient variance quadratically in α and reduces CNF solver cost roughly as $1/\alpha$ (Theorems 10–11), and we quantify robustness to curvature mis–specification (Theorem 12) and its interaction with mixed–curvature latents.

• Extensibility beyond constant curvature and practical defaults. A balanced polar pushforward theorem extends RC beyond constant curvature to any manifold with known geodesic polar volume (Theorem 3), and we outline volume–preserving Lambert–type charts on more general homogeneous (e.g. Thurston) geometries in the supplement. Across flows, VAEs, CNFs, hyperbolic graph models, and orientation models, RC integrates cleanly with existing Euclidean backbones. Within the standard wrapped–prior regime, RC–bExp emerges as a robust default choice, with RC–GCL (or RC–Exp) preferred when exact geodesics are required.

2 Background and notation

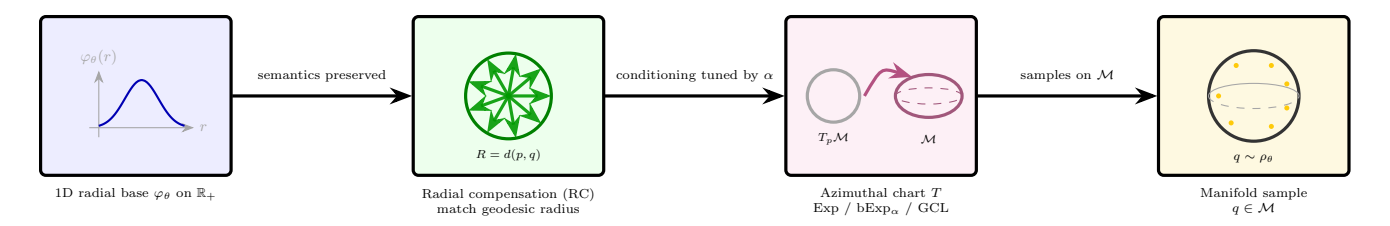


Figure 1: Conceptual RC pipeline: a 1D radial base φ_{θ} on \mathbb{R}_{+} is radially compensated so that geodesic radii R = d(p,q) preserve the target semantics, then mapped to the manifold through an azimuthal chart T (Exp / bExp $_{\alpha}$ / GCL), where the dial α tunes numerical conditioning without changing the geodesic-radial law.

Manifolds and geodesic polars. For most of the paper we work with *n*-dimensional complete, simply connected, constant–curvature Riemannian manifolds

$$M \in \left\{ \mathbb{S}_{R_c}^n, \, \mathbb{H}_{-1/R_c^2}^n \right\}$$

with curvature $\kappa \in \{+R_c^{-2}, -R_c^{-2}\}$ and a distinguished pole $p \in M$. We write

$$R = d(p, \cdot)$$

for the geodesic distance from p, and use geodesic polar coordinates $(r,\omega) \in [0,R_{\max}) \times S^{n-1}$ about p, where r = R(q) for $q \in M$, $R_{\max} = \pi R_c$ on $\mathbb{S}^n_{R_c}$ and $R_{\max} = \infty$ on \mathbb{H}^n_{-1/R_c^2} . In these coordinates the volume element factorises as

$$dvol_M = s_{\kappa}(r)^{n-1} dr d\omega, \qquad s_{\kappa}(r) = \begin{cases} R_c \sin(r/R_c), & \kappa = +R_c^{-2}, \\ R_c \sinh(r/R_c), & \kappa = -R_c^{-2}, \end{cases}$$
(1)

and we also set

$$c_{\kappa}(r) = \begin{cases} R_c \cos(r/R_c), & \kappa > 0, \\ R_c \cosh(r/R_c), & \kappa < 0. \end{cases}$$

We use x = ru with $r = ||x|| \ge 0$ and $u \in S^{n-1}$ for polar coordinates in the tangent space $T_pM \cong \mathbb{R}^n$.

More generally, on an arbitrary complete Riemannian manifold (M, g) with pole p and geodesic polar coordinates (r, ω) on a star–shaped domain, we write

$$dvol_M = J_p(r,\omega) dr d\omega (2)$$

for the polar volume element. The constant–curvature case corresponds to $J_p(r,\omega) = s_{\kappa}(r)^{n-1}$, while for general M the angular dependence of J_p captures curvature inhomogeneities. We use (2) in Sec. 3 to extend Radial Compensation beyond constant curvature via a balanced polar pushforward.

Lambert lifts and spherically symmetric charts. We call a chart spherically symmetric if its Jacobian determinant depends only on the Euclidean radius r = ||x||; in the literature this is sometimes referred to as a scalar–Jacobian azimuthal chart. Let L_p be an azimuthal equal–area (Lambert) chart centred at p, so $|\det DL_p| \equiv 1$ on its domain. For any strictly increasing C^{∞} radial profile $\rho: [0, R_{\max}) \to [0, \rho_*)$ with $\rho(0) = 0$, define the Lambert lift

$$T_{\rho}(x) = L_{p}\left(\rho(\|x\|) \frac{x}{\|x\|}\right), \quad x \in \mathbb{R}^{n}, \quad T_{\rho}(0) = p.$$
 (3)

A polar/coarea calculation yields the scalar–Jacobian identity and the radius mapping

$$\log|\det DT_{\rho}(x)| = (n-1)\log\frac{\rho(r)}{r} + \log\rho'(r), \qquad d(p, T_{\rho}(ru)) = 2\arg\left(\frac{\rho(r)}{2}\right), \tag{4}$$

with x = ru, $u \in S^{n-1}$, and

$$\operatorname{ars} = \arcsin \text{ on } \mathbb{S}^n_{R_c}, \qquad \operatorname{ars} = \operatorname{arsinh on } \mathbb{H}^n_{-1/R_c^2}.$$

These formulas reproduce the standard Lambert azimuthal equal—area identities and extend them to arbitrary curvature radius R_c ; see, e.g., [19].¹

Radial calculus. For a radial function $g: \mathbb{R}^n \to \mathbb{R}$ of the form g(x) = h(r) with x = ru, r = ||x||, $u \in S^{n-1}$,

$$\nabla g(x) = h'(r) u, \qquad \nabla^2 g(x) = h''(r) u u^\top + \frac{h'(r)}{r} (I - u u^\top).$$

We use these identities repeatedly for Lipschitz and Hessian bounds.

Units and curvature scaling. All statements below are presented for a general curvature radius R_c . Whenever unit-curvature formulas with $\kappa \in \{\pm 1\}$ appear (e.g., in local series expansions), the corresponding R_c -aware expressions are recovered by the substitutions

$$r \mapsto r/R_c, \quad s_{\kappa}(r) \mapsto R_c \, s_{\operatorname{sign}(\kappa)}(r/R_c), \quad c_{\kappa}(r) \mapsto R_c \, c_{\operatorname{sign}(\kappa)}(r/R_c).$$

3 Radial Compensation and scalar–Jacobian charts

Before giving the formal definitions, we briefly summarise the role of RC. Standard wrapped priors start from a simple Euclidean base in the tangent space and let the chart inherit whatever volume distortion the manifold geometry imposes. RC reverses this logic: we first decide what the geodesic radius R = d(p,q) should look like (e.g. "R is HalfNormal with scale 0.5") and then pre-warp the tangent space so that, after the chart, R has exactly that law and Fisher information. The rest of this section shows that, within isotropic bases and spherically symmetric charts, this is essentially the only way to keep Euclidean–style radial semantics on a curved manifold.

Within isotropic bases and scalar–Jacobian azimuthal charts, Radial Compensation (RC) is essentially the *only* way to obtain models whose likelihoods are geodesic–radial and whose Fisher information in the radial parameters is both chart– and curvature–invariant (Theorem 4, Corollary 1). Any other base in this modelling class must break at least one of these invariances; see the impossibility triangle in Fig. 4.

¹We follow the notation s_{κ} and c_{κ} for spherical and hyperbolic sine/cosine factors and use the azimuthal Lambert–lift construction throughout.

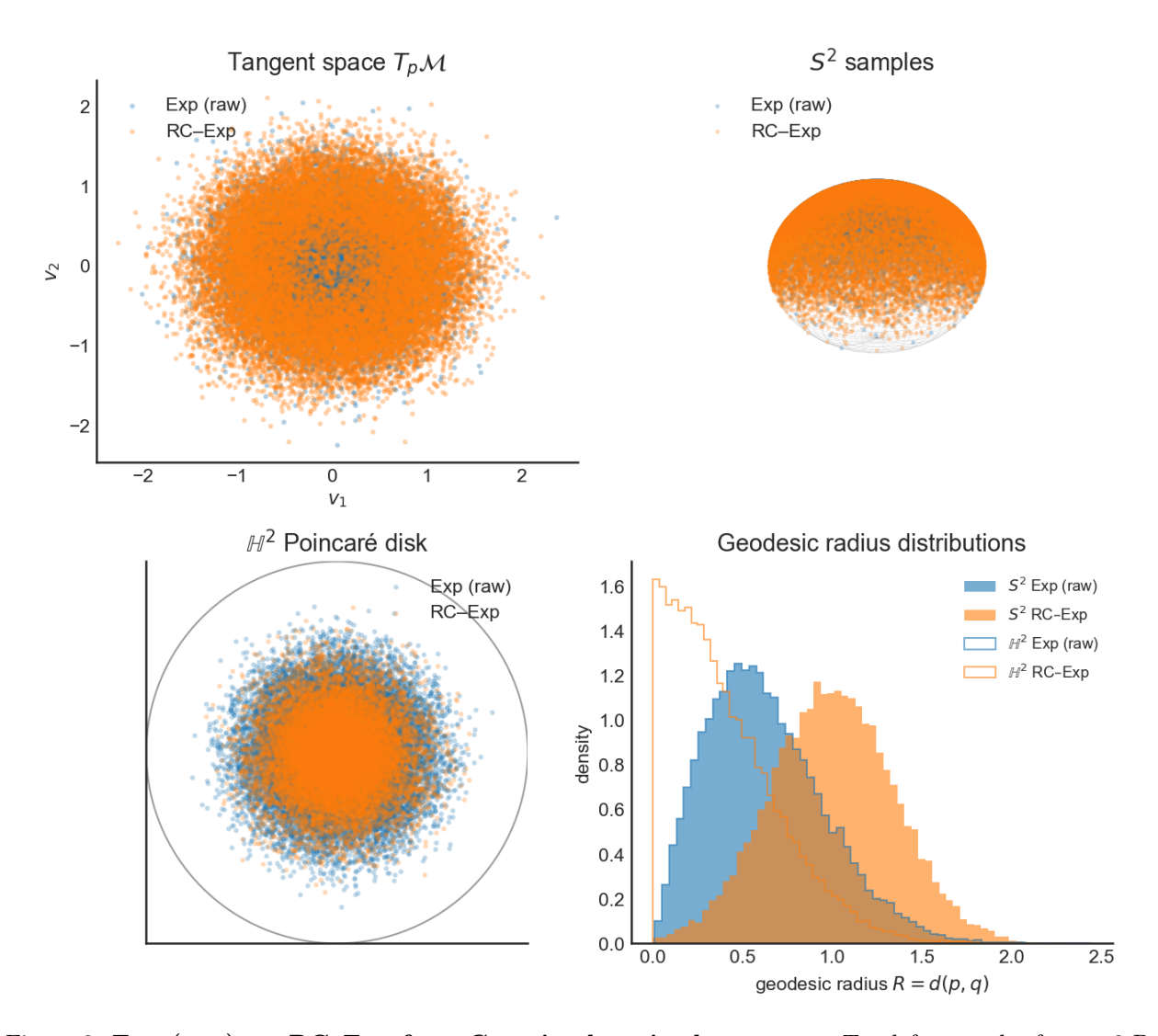


Figure 2: Exp (raw) vs. RC-Exp for a Gaussian base in the tangent. Top left: samples from a 2-D isotropic Gaussian in the tangent plane T_pM . Both constructions start from the same Euclidean base; the labels EXP (RAW) and RC-EXP indicate only which chart is used downstream. Top right: pushforward of these samples to the sphere \mathbb{S}^2 via the exponential map. The standard wrapped Gaussian obtained with EXP (RAW) concentrates mass closer to the pole, shrinking the intended cap and pulling the geodesic radius R = d(p,q) to smaller mean and variance, whereas RC-ExP yields a thicker cap at the prescribed geodesic scale. Bottom left: the same experiment on hyperbolic space \mathbb{H}^2 , visualised in the Poincaré disk. Here EXP (RAW) pushes mass further out, producing heavier tails and larger mean radius, while RC-EXP concentrates samples near the target scale. Bottom right: histograms of R = d(p,q) on \mathbb{S}^2 and \mathbb{H}^2 . Under RC-EXP the empirical law of R matches the chosen one-dimensional radial target (same mean and variance in geodesic units), whereas EXP (RAW) exhibits curvature-induced distortions due to the polar factor $(s_{\kappa}(R)/R)^{n-1}$. In particular, a parameter σ that is intended to control geodesic spread implicitly depends on curvature, dimension, and chart, undermining hyperparameter transfer across geometries.

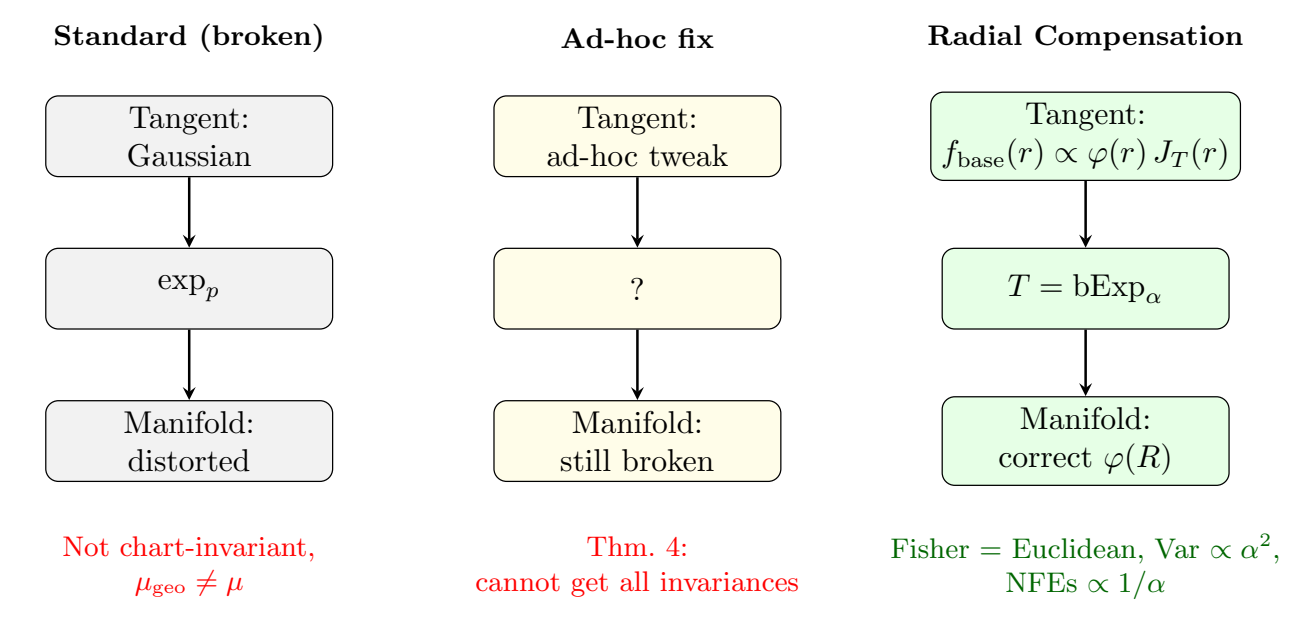


Figure 3: Conceptual comparison of standard wrapped priors, ad-hoc fixes, and Radial Compensation (RC). Within the isotropic spherically symmetric (scalar–Jacobian) class, only RC simultaneously yields geodesic–radial models and chart–invariant Fisher information for the radial parameters (Theorem 4).

Isotropic scalar-Jacobian

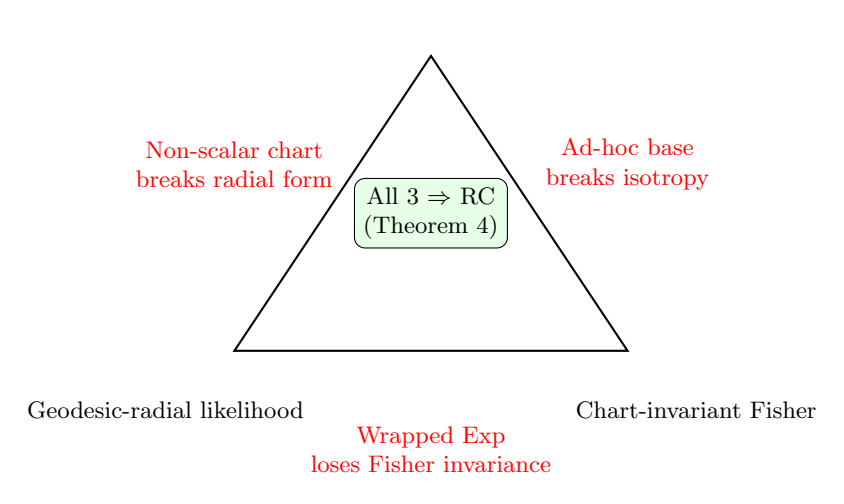


Figure 4: Impossibility triangle. Within isotropic scalar–Jacobian models, any chart/base pair can satisfy at most two of: (i) geodesic–radial likelihoods, (ii) chart–invariant Fisher information in radial parameters, (iii) isotropy in the tangent space. RC is the unique way to realise all three simultaneously.

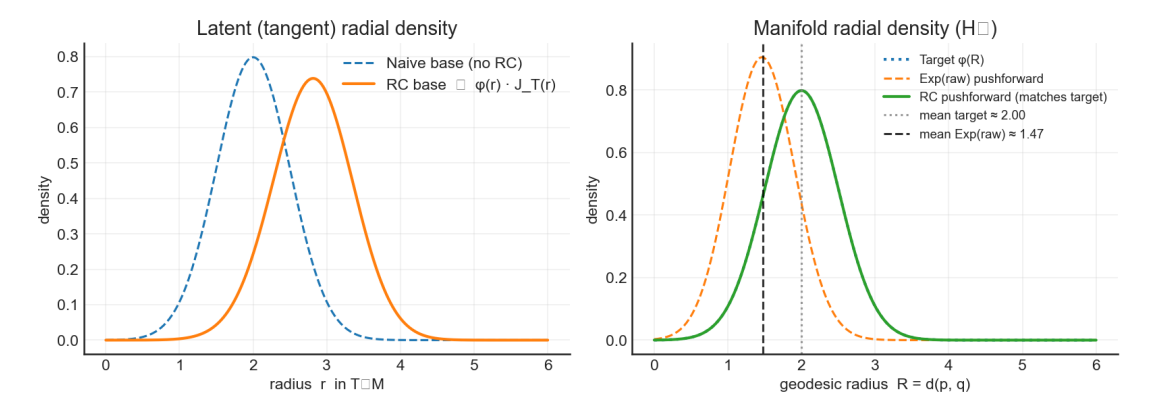


Figure 5: Radial Compensation as a pre-warped prior. Left: in the tangent space, RC (orange) multiplies the target radial law $\phi(r)$ by the chart Jacobian $J_T(r)$, pushing mass outward and thickening the tails relative to the naive Euclidean base (blue dashed). Right: on hyperbolic space H^n , the naive Exp (RAW) pushforward (orange dashed) is pulled toward the pole, with geodesic mean ≈ 1.47 instead of the intended ≈ 2.0 . RC cancels the hyperbolic volume factor, so its pushforward (green) coincides with the target manifold radial law $\phi(R)$ (dotted), preserving parameter semantics (mean and scale) in geodesic units. RC takes the complexity hit in the latent space so that the manifold distribution remains simple and statistically meaningful.

Figure 2 illustrates how Radial Compensation restores parameter semantics for wrapped Gaussians on curved spaces. All four panels start from the same 2-D Gaussian base in the tangent plane T_pM ; the only difference is whether samples are pushed to the manifold with the uncorrected exponential map (EXP (RAW)) or with its radially compensated version (RC-EXP). On \mathbb{S}^2 , the raw exponential map shrinks the spherical cap toward the pole, so the geodesic radius R = d(p,q) has substantially smaller mean and variance than intended. On \mathbb{H}^2 the opposite happens: EXP (RAW) produces a heavier-tailed cloud with radii systematically larger than the target scale. Under RC-EXP, the samples on both \mathbb{S}^2 and \mathbb{H}^2 occupy the intended geodesic annulus, and the histograms of R match the chosen one-dimensional radial law up to sampling noise.

Standard azimuthal charts warp space: an isotropic Gaussian in the tangent, when pushed through the exponential map, becomes a spherical cap whose geodesic radii are systematically *shrunk* on \mathbb{S}^n and *expanded* on \mathbb{H}^n (Fig. 2, Fig. 5). RC fixes this by pre-warping the base distribution.

In the tangent, we multiply the target radial law $\phi_{\theta}(r)$ by the chart Jacobian $J_T(r)$, pushing mass outward or inward in exactly the opposite direction of the chart's distortion (Fig. 5, left). After pushing this RC-corrected base through the chart, the geodesic radius R = d(p,q) on the manifold has exactly the law $\phi_{\theta}(R)$ we started from (Fig. 5, right).

Intuitively, RC takes the complexity hit in the latent space so that the manifold distribution retains simple one-dimensional semantics, "mean stays mean, variance stays variance", in geodesic units.

Scalar–Jacobian charts. A chart $T: \mathbb{R}^n \to M$ (about p) is scalar–Jacobian if its log–Jacobian determinant depends only on the Euclidean radius r = ||x||:

$$\log |\det DT(x)| = \psi(||x||), \quad x \in \mathbb{R}^n,$$

for some scalar profile ψ . Lambert lifts T_{ρ} in (3) are canonical representatives of this class (see Sec. 4).

Radial Compensation (RC) for scalar–Jacobian charts. Fix any target one–dimensional radial density ϕ_{θ} on $[0, R_{\text{max}})$, with parameter θ . For a scalar–Jacobian chart T with radial Jacobian factor

$$J_T(r) := \exp(\psi(r)),$$

we define the RC base in $T_pM \cong \mathbb{R}^n$ via its radial density

$$f_{\theta}^{\text{base}}(r) \propto \phi_{\theta}(r) J_T(r), \qquad \Omega \sim \text{Unif}(S^{n-1}), \quad X = r\Omega, \quad Q = T(X).$$
 (5)

Equivalently, X is sampled in polar coordinates with radial law f_{θ}^{base} and uniform direction, and then mapped to M by T.

Theorem 1 (RC invariances: likelihood, Fisher, and KL). Let T be a scalar–Jacobian chart about p and let the RC base be defined by (5). Then the pushforward density on M is

$$\rho_{\theta}(q) = \phi_{\theta}(R), \qquad R = d(p, q),$$

so each sample enters the likelihood only through its geodesic radius R. Moreover, for the radial parameter θ ,

$$I_M(\theta) = I_{\mathbb{R}^1}(\theta), \quad \mathrm{KL}(\rho_{\theta} \| \rho_n) = \mathrm{KL}(\phi_{\theta} \| \phi_n),$$

provided $\{\log \phi_{\theta}\}$ admits an integrable envelope so that differentiation under the manifold integral is justified by dominated convergence.

Remark 1 (Scope). The invariances in Theorem 1 hold for the RC base family parameters θ . They do not claim model-level Fisher invariance under arbitrary downstream learnable transforms: blocks with unit Jacobian preserve Fisher, but general learnable charts/flows need not.

Theorem 2 (Chart–invariance within the scalar–Jacobian class). Let T, S be two scalar–Jacobian azimuthal charts centred at p, each equipped with its own RC base as in (5). Then

$$\rho_{\theta}^T(q) \ = \ \rho_{\theta}^S(q) \ = \ \phi_{\theta}\big(d(p,q)\big), \qquad I_M^T(\theta) \ = \ I_M^S(\theta) \ = \ I_{\mathbb{R}^1}(\theta).$$

Optimisation trajectories may differ because the Euclidean pre-flows feeding T or S are parametrised differently, but optima and asymptotic covariances in θ coincide.

RC on general manifolds via balanced polar pushforward. The scalar–Jacobian construction above assumes that the chart Jacobian collapses to a radial factor. A key conceptual point is that an analogous recipe exists on any manifold where geodesic polar coordinates and the polar volume element J_p in (2) are known.

Theorem 3 (Balanced polar pushforward on general manifolds). Let (M,g) be a complete Riemannian manifold, $p \in M$ a pole, and suppose that on a star-shaped geodesic domain about p we have polar coordinates (r,ω) with $d\mathrm{vol}_M = J_p(r,\omega) \, dr \, d\omega$. Fix a one-dimensional radial family $\{\phi_\theta\}$ on $[0,R_{\mathrm{max}})$ and define a balanced polar base on T_pM in polar coordinates (r,ω) by

$$f_{\theta}^{\text{bal}}(r,\omega) \propto \phi_{\theta}(r) J_{p}(r,\omega), \qquad V \sim f_{\theta}^{\text{bal}}, \quad Q = \exp_{p}(V).$$

Then on the image of the star domain,

$$\rho_{\theta}(q) = \phi_{\theta}(d(p,q))$$

with respect to $dvol_M$, so the geodesic radius R = d(p,Q) has law ϕ_{θ} . If sectional curvatures are bounded and J_p is C^3 in r, then on geodesic balls of radius R the Fisher information satisfies

$$||I_M(\theta) - I_{\mathbb{R}^1}(\theta)|| \le C(n) \sup_{\|v\| \le R} |\partial_r^3 \log J_p(r,\omega)| R^3,$$

with equality $I_M(\theta) = I_{\mathbb{R}^1}(\theta)$ whenever J_p depends only on r (e.g., constant-curvature spaces).

This shows that RC is not a sphere/hyperbolic trick but a general recipe applicable to any manifold with a known polar volume element $J_p(r,\omega)$, including rank—one symmetric spaces and other homogeneous manifolds. On $\mathbb{S}^n_{R_c}$ and \mathbb{H}^n_{-1/R_c^2} , Theorem 3 recovers our RC–Exp construction with $J_p(r,\omega) = s_\kappa(r)^{n-1}$ and shows that RC is not specific to constant curvature but a general information—geometric recipe for building geodesic—radial families on manifolds with known polar volume.

Uniqueness of RC within isotropic scalar—Jacobian bases. The next result upgrades RC from "a convenient choice" to an essentially unique construction within the natural modelling class we consider.

Theorem 4 (Characterization of RC). Let M be a constant-curvature manifold, $T: \mathbb{R}^n \to M$ a scalar-Jacobian azimuthal chart about p, and consider isotropic tangent densities $f_{\theta}(x) = h_{\theta}(\|x\|)$, $\theta \in \Theta$. Assume that there exists a radial family $\{\phi_{\theta}\}$ on $[0, R_{\max})$ such that, for all θ :

- 1. the pushforward density is geodesic-radial, $\rho_{\theta}(q) = \phi_{\theta}(d(p,q))$,
- 2. the Fisher information for θ is chart-invariant and matches the 1D radial Fisher, $I_M(\theta) = I_{\mathbb{R}^1}(\theta)$.

Then, up to a smooth reparametrisation of θ , the only such base family is the RC base (5):

$$h_{\theta}(r) \propto \phi_{\theta}(r) J_T(r).$$

In other words, within isotropic bases and scalar–Jacobian azimuthal charts, RC is essentially the unique way to obtain Euclidean–like parameter semantics on M.

Informally, Theorem 4 says that once we insist on isotropy and a spherically symmetric chart, RC is the only way to make the radial parameter θ "look Euclidean" on every manifold and every chart. Figure 4 summarises this as an impossibility triangle: within isotropic scalar—Jacobian models, the only way to simultaneously realise geodesic—radial likelihoods and chart—invariant Fisher information is to use Radial Compensation.

Corollary 1 (RC uniquely realises chart- and curvature-invariant radial semantics). Let $M \in \{\mathbb{S}^n_{Rc}, \mathbb{H}^n_{-1/R_c^2}\}$ be a constant-curvature manifold with pole $p \in M$, and let R = d(p,q) denote the geodesic radius. Fix a one-dimensional radial family $\{\varphi_{\vartheta}\}_{\vartheta \in \Psi}$ on $[0,R_{\max})$. Consider models obtained by pushing isotropic bases $f_{\theta}^{(T)}(x) = h_{\theta}^{(T)}(\|x\|)$, $\theta \in \Theta \subset \mathbb{R}^m$, through scalar-Jacobian azimuthal charts $T : \mathbb{R}^n \to M$ about p. We say that such a collection $\{\rho_{\theta}^{(T)}\}_{T,\theta}$ achieves Goal \mathcal{G} if there exists a smooth bijection $\vartheta = \psi(\theta)$ such that, for every scalar-Jacobian chart T and every $\theta \in \Theta$:

(1) Exact radial semantics:

$$\rho_{\theta}^{(T)}(q) = \varphi_{\psi(\theta)}(d(p,q))$$
 for all $q \in M$,

i.e. the manifold likelihood depends on q only through its geodesic radius R = d(p,q) with a chart-independent radial law φ_{ϑ} ;

(2) Chart- and curvature-invariant Fisher: the Fisher information of ϑ under $\rho_{\theta}^{(T)}$ coincides with the one-dimensional radial Fisher information and does not depend on T:

$$I_M^{(T)}(\vartheta) \ = \ I_{\mathbb{R}^1}(\vartheta) \ := \ \mathbb{E}_{\vartheta} \big[\nabla_{\vartheta} \log \varphi_{\vartheta}(R) \, \nabla_{\vartheta} \log \varphi_{\vartheta}(R)^\top \big] \qquad \textit{for all scalar-Jacobian charts T.}$$

Then, within the class of isotropic bases and scalar-Jacobian azimuthal charts, the following hold:

1. (Existence via RC) For any scalar-Jacobian chart T with radial Jacobian factor $J_T(r) = \exp\{\psi_T(r)\}\$, the Radial Compensation (RC) base

$$h_{\theta}^{(T)}(r) \propto \varphi_{\psi(\theta)}(r) J_T(r)$$

(equation (5)) induces pushforward densities

$$\rho_{\theta}^{(T)}(q) = \varphi_{\psi(\theta)}(d(p,q)),$$

and Fisher information $I_M^{(T)}(\vartheta) = I_{\mathbb{R}^1}(\vartheta)$. Moreover, by Theorem 2, the resulting $\rho_{\theta}^{(T)}$ and $I_M^{(T)}(\vartheta)$ are independent of the particular scalar–Jacobian chart T. Hence RC achieves Goal \mathcal{G} .

2. (Impossibility without RC) Conversely, suppose a collection $\{\rho_{\theta}^{(T)}\}_{T,\theta}$ built from isotropic bases and scalar–Jacobian charts satisfies Goal \mathcal{G} . Fix any such chart T and write its base as $f_{\theta}^{(T)}(x) = h_{\theta}(\|x\|)$. Then there exists a smooth bijection $\vartheta = \psi(\theta)$ such that

$$\rho_{\theta}^{(T)}(q) = \varphi_{\psi(\theta)}(d(p,q)), \qquad I_M^{(T)}(\vartheta) = I_{\mathbb{R}^1}(\vartheta),$$

so assumptions (1)-(2) of Theorem 4 (Characterization of RC) are satisfied for the isotropic family f_{θ} in the chart T. By Theorem 4, the base must therefore be of RC form,

$$h_{\theta}(r) \propto \varphi_{\psi(\theta)}(r) J_T(r),$$

up to a smooth reparametrisation of θ . Since T was arbitrary, every scalar–Jacobian chart in the model must use an RC base. In particular, within this modelling regime there is no non-RC construction that can satisfy Goal \mathcal{G} .

Proof. For part (a), fix a scalar–Jacobian chart T with radial Jacobian factor $J_T(r)$. Define the RC base in $T_nM \cong \mathbb{R}^n$ by

$$f_{\theta}^{\text{RC}}(x) \propto \varphi_{\psi(\theta)}(\|x\|) J_T(\|x\|)$$
 as in (5).

Theorem 1 (RC invariances) then yields

$$\rho_{\theta}^{(T)}(q) = \varphi_{\psi(\theta)}(d(p,q)), \qquad I_{M}^{(T)}(\vartheta) = I_{\mathbb{R}^{1}}(\vartheta),$$

so both items of Goal \mathcal{G} hold for this chart. Theorem 2 (chart–invariance within the scalar–Jacobian class) shows that these densities and Fisher information do not depend on which scalar–Jacobian chart is used, so RC achieves Goal \mathcal{G} .

For part (b), assume a model in the isotropic + scalar–Jacobian class achieves Goal \mathcal{G} . Fix a scalar–Jacobian chart T and write its isotropic tangent base as $f_{\theta}(x) = h_{\theta}(\|x\|)$. By Goal \mathcal{G} there exists a smooth bijection $\theta = \psi(\theta)$ such that

$$\rho_{\theta}^{(T)}(q) = \varphi_{\psi(\theta)}(d(p,q)), \qquad I_{M}^{(T)}(\vartheta) = I_{\mathbb{R}^{1}}(\vartheta),$$

for all θ . These are exactly conditions (1)–(2) in Theorem 4 for the chart T and the radial family $\{\varphi_{\vartheta}\}$. Applying Theorem 4 (*Characterization of RC*) therefore yields

$$h_{\theta}(r) \propto \varphi_{\psi(\theta)}(r) J_T(r),$$

up to a smooth reparametrisation of θ , i.e. the base in T is of RC form. Because T was arbitrary, the same conclusion holds for every scalar–Jacobian chart in the collection. Thus no non–RC isotropic base can satisfy Goal \mathcal{G} , proving the claimed impossibility.

Statistical consequences of RC. The RC and balanced polar constructions have clean information—geometric consequences. Under mild regularity (identifiability, differentiability under the integral, dominated scores), if $Q \sim \rho_{\theta} d\text{vol}_M$ with $\rho_{\theta}(q) = \phi_{\theta}(d(p,q))$ as above, then:

- The Fisher cross–information between θ and the pole p vanishes, $I(\theta, p) = 0$, so statistical uncertainty in parameters and geometry decouples.
- The Fisher information in θ matches the Euclidean radial Fisher: $I_M(\theta) = I_{\mathbb{R}^1}(\theta)$ (exactly in the constant–curvature case, and up to curvature–controlled error in the general case of Theorem 3).
- The MLE $\hat{\theta}_n$ is consistent and satisfies the usual CLT, $\sqrt{n}(\hat{\theta}_n \theta_0) \Rightarrow \mathcal{N}(0, I_{\mathbb{R}^1}(\theta_0)^{-1})$, so asymptotic efficiency and covariance are exactly those of the corresponding 1D Euclidean radial model.

For optimisation, these Fisher properties imply that the scale of gradients in θ , and the asymptotic conditioning of the log-likelihood, remain the same as for the underlying one-dimensional Euclidean radial model, *independent of curvature or chart*. In particular, changing the curvature or replacing Exp by bExp or GCL does not alter the Fisher-optimal learning rates for θ ; the only change in conditioning arises from the

chart term, which we analyse in Theorems 10 and 11.

Thus RC makes the parameter manifold in θ effectively flat in the Fisher metric and separates "what the parameters mean" from curvature and chart choices.

Corollary 2 (RC is necessary and sufficient for Fisher-efficient radial learning). Let $M \in \{\mathbb{S}_{R_e}^n, \mathbb{H}_{-1/R^2}^n\}$ be a constant-curvature manifold with pole $p \in M$, and let $T : \mathbb{R}^n \to M$ be a scalar-Jacobian azimuthal chart about p with radial Jacobian factor $J_T(r) = \exp(\psi(r))$. Consider isotropic tangent densities $f_{\theta}(x) = h_{\theta}(\|x\|)$, $\theta \in \Theta \subset \mathbb{R}^m$, and write $\rho_{\theta}^{(T)}$ for the corresponding pushforward density on M. Suppose there exist a one-dimensional radial family $\{\varphi_{\vartheta}\}_{\vartheta \in \Psi}$ on $[0,R_{\max})$ and a smooth reparametrisation

 $\vartheta = \psi(\theta)$ such that, for every $\theta \in \Theta$,

(1) Geodesic-radial form:

$$\rho_{\theta}^{(T)}(q) = \varphi_{\psi(\theta)}(R), \qquad R = d(p, q),$$

so the likelihood depends on q only through its geodesic radius R;

(2) Fisher-efficient rates: the Fisher information for ϑ on M coincides with the one-dimensional radial Fisher information,

$$I_M(\vartheta) = I_{\mathbb{R}^1}(\vartheta) := \mathbb{E}_{\vartheta} [\nabla_{\vartheta} \log \varphi_{\vartheta}(R) \nabla_{\vartheta} \log \varphi_{\vartheta}(R)^{\top}].$$

Then:

1. (Necessity) Up to a smooth reparametrisation of θ , the tangent base must be the RC base, in the sense that

$$h_{\theta}(r) \propto \varphi_{\psi(\theta)}(r) J_T(r),$$

i.e. Radial Compensation is necessary within isotropic scalar-Jacobian models for simultaneously obtaining geodesic-radial likelihoods and Euclidean one-dimensional Fisher information in geodesic

2. (Sufficiency) Conversely, for any one-dimensional radial family $\{\varphi_{\vartheta}\}$ and any scalar-Jacobian chart T, define the RC base in $T_pM \cong \mathbb{R}^n$ by

$$f_{\vartheta}^{\mathrm{RC}}(x) \propto \varphi_{\vartheta}(\|x\|) J_T(\|x\|).$$

Then the pushforward density satisfies

$$\rho_{\vartheta}^{(T)}(q) = \varphi_{\vartheta}(d(p,q)), \qquad I_{M}(\vartheta) = I_{\mathbb{R}^{1}}(\vartheta).$$

Under the regularity assumptions stated above, the MLE $\hat{\vartheta}_n$ based on i.i.d. samples from $\rho_{\vartheta_0}^{(T)}$ is asymptotically normal with Euclidean covariance,

$$\sqrt{n} \left(\hat{\vartheta}_n - \vartheta_0 \right) \Rightarrow \mathcal{N} \left(0, I_{\mathbb{R}^1} (\vartheta_0)^{-1} \right).$$

The previous result has an important implication: whenever the data are generated from an RC model, any KL-consistent chart-based learner operating within our modelling class is forced to recover RC in the limit.

Theorem 5 (Implicit RC from likelihood matching). Let $M \in \{\mathbb{S}^n_{R_c}, \mathbb{H}^n_{-1/R_c^2}\}$ be a constant-curvature manifold with pole $p \in M$, and let $T : \mathbb{R}^n \to M$ be a scalar-Jacobian azimuthal chart about p with radial Jacobian factor $J_T(r) = \exp\{\psi(r)\}$. Let $\{\varphi_{\vartheta}\}_{{\vartheta}\in\Psi}$ be a one-dimensional radial family on $[0,R_{\max})$, and let

$$\rho^{\star}(q) = \varphi_{\vartheta^{\star}}(d(p,q))$$

be an RC model on M for some $\vartheta^* \in \Psi$, obtained via the RC construction in any scalar-Jacobian chart (so that Theorems 1–2 apply).² Now consider an arbitrary isotropic tangent family $f_{\theta}(x) = h_{\theta}(||x||), \ \theta \in \Theta$, pushed forward through T to densities $\rho_{\theta}^{(T)}$ on M. Assume that there exists a smooth reparametrisation $\vartheta = \psi(\theta)$ such that, for all $\theta \in \Theta$:

²By Theorem 2, the particular scalar–Jacobian chart used to define ρ^* is immaterial: all such charts induce the same geodesic-radial law $\rho^*(q) = \varphi_{\vartheta^*}(d(p,q))$ and the same Fisher information in ϑ .

(1) **Geodesic-radial form.** The pushforward is geodesic-radial with respect to $\{\varphi_{\vartheta}\}$,

$$\rho_{\theta}^{(T)}(q) = \varphi_{\psi(\theta)}(R), \qquad R = d(p,q).$$

(2) **Euclidean radial Fisher.** The Fisher information in ϑ under $\rho_{\theta}^{(T)}$ coincides with the one-dimensional radial Fisher,

$$I_M(\vartheta) = I_{\mathbb{R}^1}(\vartheta) := \mathbb{E}_{\vartheta} [\nabla_{\vartheta} \log \varphi_{\vartheta}(R) \nabla_{\vartheta} \log \varphi_{\vartheta}(R)^{\top}],$$

where $R \sim \varphi_{\vartheta}$.

Define the population KL objective

$$L(\theta) := \mathbb{E}_{Q \sim \rho^{\star}} \left[-\log \rho_{\theta}^{(T)}(Q) \right] = \mathrm{KL}(\rho^{\star} \parallel \rho_{\theta}^{(T)}) + const.$$

Assume that:

- the radial family $\{\varphi_{\vartheta}\}$ is identifiable (i.e., $\varphi_{\vartheta} = \varphi_{\vartheta'}$ implies $\vartheta = \vartheta'$), and
- there exists at least one $\theta^* \in \Theta$ such that $L(\theta^*) = \inf_{\theta \in \Theta} L(\theta)$ and $KL(\rho^* \parallel \rho_{\theta^*}^{(T)}) = 0$.

Then:

(i) (Implicit RC at the KL minimiser) At any such minimiser θ^* one has

$$\rho_{\theta^{\star}}^{(T)}(q) = \rho^{\star}(q) \quad for \, dvol_M \text{-}a.e. \, q,$$

and the corresponding tangent base must be an RC base (up to smooth reparametrisation):

$$h_{\theta^*}(r) \propto \varphi_{\psi(\theta^*)}(r) J_T(r).$$

In particular, within isotropic bases and scalar–Jacobian charts satisfying (1)–(2), any model that perfectly matches a geodesic–radial RC target via KL minimisation is forced to implement RC at the optimum.

(ii) (Implicit RC for KL-consistent estimators) Let $\hat{\theta}_n$ be any sequence of estimators that approximately minimises the empirical negative log-likelihood

$$L_n(\theta) := \frac{1}{n} \sum_{i=1}^n -\log \rho_{\theta}^{(T)}(Q_i), \quad Q_i \stackrel{i.i.d.}{\sim} \rho^{\star},$$

in the sense that $\hat{\theta}_n \to \theta^*$ in probability (KL-consistency). Under the regularity conditions used in the "Statistical consequences of RC" paragraph, $\rho_{\hat{\theta}_n}^{(T)} \to \rho^*$ in probability and the associated tangent bases converge to the RC base at θ^* . Thus any KL-consistent learning procedure within this modelling class implicitly learns RC whenever the data are generated from an RC model.

Sampling under RC. Sampling from an RC model is particularly simple: draw $R \sim \phi_{\theta}$ on $[0, R_{\text{max}})$ and $\Omega \sim \text{Unif}(S^{n-1})$, set $X = R\Omega$, and output Q = T(X). Then d(p, Q) = R and the resulting density on M satisfies $\rho_{\theta}(q) = \phi_{\theta}(d(p, q))$ (with truncation at R_{max} on $\mathbb{S}^n_{R_c}$).

Algorithm 1 SampleRC(ϕ_{θ} , T)

- 1: Sample $R \sim \phi_{\theta}$ on $[0, R_{\text{max}})$ and $\Omega \sim \text{Unif}(S^{n-1})$.
- 2: Set $Q \leftarrow T(R\Omega)$ and **return** Q.

Charts used in this paper. We instantiate RC with the following scalar–Jacobian charts:

- Exp: the exponential chart $T = \exp_p$ with $\log |\det DT(x)| = (n-1)\log(s_{\kappa}(r)/r)$.
- $b \text{Exp}_{\alpha}$: the balanced–exponential chart $T = T_{\rho_{\alpha}}$ (Sec. 4) with scalar log–det $\log |\det DT(x)| = (n-1)\alpha \log(s_{\kappa}(r)/r)$, which interpolates between an equal–area profile ($\alpha = 0$) and the exponential chart ($\alpha = 1$).
- GCL: the geodesic-corrected Lambert chart with exact geodesic radii and scalar log-det (Sec. 4).

All three charts belong to the scalar–Jacobian class, so under RC they induce the same geodesic–radial density and Fisher information; they differ only in their Jacobian bookkeeping and associated optimisation behaviour.

4 Main results

We now make precise the structure of the scalar—Jacobian charts used in our constructions, the variational characterization of the Balanced–Exponential (bExp) family, and the properties of our Geodesic–Corrected Lambert (GCL) chart and atlas. Finally, we connect these geometric results to training-relevant quantities such as gradient variance and CNF solver complexity.

4.1 Complete class: scalar–Jacobian azimuthal \iff Lambert–lifts

Proposition 1 (Representation of scalar–Jacobian azimuthal charts). Let $M \in \{\mathbb{S}^n_{R_c}, \mathbb{H}^n_{-1/R_c^2}\}$ and $p \in M$. If a smooth azimuthal chart $T : \mathbb{R}^n \to M$ about p satisfies $\log |\det DT(x)| = \psi(\|x\|)$ for some scalar profile ψ , then there exists a strictly increasing C^{∞} radial profile $\rho : [0, R_{\max}) \to [0, \rho_*)$ with $\rho(0) = 0$ such that

$$T(x) = L_p\left(\rho(\|x\|) \frac{x}{\|x\|}\right) =: T_\rho(x),$$

and T_{ρ} satisfies the scalar Jacobian and radius identities in (4).

Thus every scalar–Jacobian azimuthal chart is a Lambert–lift for some profile ρ . Designing scalar–Jacobian charts reduces to choosing ρ .

4.2 Balanced-Exponential (bExp): integral solution, existence, and optimality

Definition and integral solution. Within the Lambert-lift class T_{ρ} , bExp charts interpolate between equal-area Lambert and the exponential map via a single dial $\alpha \in [0, 1]$. For $\alpha \in [0, 1]$, define ρ_{α} by

$$\left(\frac{\rho_{\alpha}(r)}{r}\right)^{n-1} \rho_{\alpha}'(r) = \left(\frac{s_{\kappa}(r)}{r}\right)^{(n-1)\alpha}, \quad \rho_{\alpha}(0) = 0, \ \rho_{\alpha}'(0) = 1, \tag{6}$$

$$\rho_{\alpha}(r) = \left[n \int_{0}^{r} t^{(n-1)(1-\alpha)} s_{\kappa}(t)^{(n-1)\alpha} dt \right]^{1/n}.$$
 (7)

Theorem 6 (Existence, monotonicity, invertibility, scalar log-det). For every $\alpha \in [0,1]$, the profile ρ_{α} in (6)–(7) is C^{∞} , strictly increasing on (0, R_{\max}), and defines a C^{∞} diffeomorphism $T_{\alpha} := T_{\rho_{\alpha}}$ from a star domain onto its image. On \mathbb{H}^n_{-1/R_c^2} it is global; on $\mathbb{S}^n_{R_c}$ it is a diffeomorphism on $\{r < R_{\max}\}$. Moreover, for $x \neq 0$ with r = ||x||,

$$\log |\det DT_{\alpha}(x)| = (n-1)\alpha \log \frac{s_{\kappa}(r)}{r}.$$

Proposition 2 (Local series, mismatch, and α -monotonicity). As $r \downarrow 0$,

$$\rho_{\alpha}(r) = r \left[1 - \frac{(n-1)\alpha \kappa}{6(n+2)R_c^2} r^2 + O(r^4) \right], \qquad d(p, T_{\alpha}(ru)) = r + O(\kappa r^3/R_c^2),$$

and the geodesic mismatch $|d(p,T_{\alpha}(ru))-r|$ is nonincreasing in α and vanishes as $\alpha \uparrow 1$.

Thus α controls how the chart trades geodesic fidelity against Jacobian regularity: $\alpha = 1$ recovers the exponential chart, while $\alpha = 0$ recovers Lambert.

Within the Lambert–lift class, bExp charts are therefore the *Goldilocks profiles*: they trade off volume distortion and geodesic error in a principled way controlled by a single dial α .

Theorem 7 (Variational optimality and Pareto frontier). Among Lambert–lifts T_{ρ} , the profile ρ_{α} uniquely minimizes the strictly convex functional

$$\mathcal{E}_{\alpha}(\rho) = (1-\alpha) \int r^{n-1} ((n-1) \log \frac{\rho(r)}{r} + \log \rho'(r))^2 dr + \alpha \int r^{n-1} (G(\rho(r)) - r)^2 dr,$$

with $G(\rho) = 2 \operatorname{ars}(\rho/2)$, subject to $\rho(0) = 0$, $\rho'(0) = 1$ and admissible boundary conditions at R_{\max} . Thus α parametrizes the lower Pareto frontier between volume distortion and geodesic error within the scalar–Jacobian class.

In other words, among all scalar—Jacobian azimuthal charts, bExp is the unique "just-right" family that parametrizes the lower Pareto frontier between geodesic fidelity and Jacobian regularity.

Proposition 3 (Bi–Lipschitz control on compact shells). Let $A_{\delta,R} := \{x : \delta \leq ||x|| \leq R < R_{\max}\}$. There exist constants $m_{\alpha}, L_{\alpha} > 0$ (explicit in $\inf_{A_{\delta,R}} \rho'_{\alpha}$ and $\sup_{A_{\delta,R}} \rho'_{\alpha}$) such that

$$m_{\alpha}||x-y|| \leq d(T_{\alpha}(x), T_{\alpha}(y)) \leq L_{\alpha}||x-y||, \quad x, y \in A_{\delta,R}.$$

Combined with Theorems 1–2, these results show that RC-bExp provides a one-parameter family of charts that leaves the geodesic-radial likelihood and Fisher information invariant, while smoothly tuning geometric conditioning.

4.3 GCL: geodesic-exact Lambert-lift

Theorem 8 (GCL is geodesic–exact with scalar log-det). Let $\Phi(r) = 2 s_{\kappa}(r/2)$ and $\mathcal{G}(x) = L_p(\Phi(||x||) x/||x||)$, and write r = ||x||. Then

$$d(p, \mathcal{G}(x)) = ||x||, \qquad \log|\det D\mathcal{G}(x)| = (n-1)\log \frac{s_{\kappa}(r/2)}{r/2} + \log c_{\kappa}(r/2).$$

Any geodesic-preserving Lambert-lift with a scalar radial Jacobian coincides with \mathcal{G} .

Proposition 4 (No free lunch & near-cut blow-up). If $\kappa \neq 0$, no azimuthal chart is simultaneously unit-volume and geodesic-preserving. For geodesic-preserving charts on $\mathbb{S}_{R_n}^n$ (e.g., \mathcal{G}),

$$\|\nabla_x \log|\det DT(x)|\| \gtrsim \frac{c}{\pi R_c - r}$$
 as $r \uparrow \pi R_c$.

GCL is therefore the unique geodesic-exact Lambert–lift with a scalar Jacobian, but necessarily inherits near-cut-locus stiffness.

4.4 Atlas regularity on \mathbb{S}^n

Theorem 9 (Two-chart atlas with smooth gate is C^1 globally). On $\mathbb{S}^n_{R_c}$, use antipodal azimuthal charts with a C^{∞} partition of unity that vanishes within distance δ of each pole's cut locus. Then the per-sample log-likelihood is C^1 (and C^2 if the Euclidean backbone is C^2), with $\|\nabla \log p\|$ and $\|\nabla^2 \log p\|$ uniformly bounded on compacta away from the seams.

This construction yields a simple atlas that avoids cut loci while keeping objectives globally smooth when combined with standard Euclidean backbones.

4.5 Training-relevant variance and CNF complexity

Building on the Fisher-flatness of RC in §3, we now quantify how the bExp dial α affects gradient variance and the stiffness of coordinate-based CNFs, under the assumption that RC is used so that the underlying likelihood does not change with α .

Theorem 10 (Chart–term variance and gradient bound). Let Q be distributed under any RC model and let T_{α} be the bExp chart. Writing R = d(p, Q),

$$\operatorname{Var}\left[\log|\det DT_{\alpha}^{-1}(Q)|\right] = \alpha^{2}\operatorname{Var}\left[(n-1)\log\frac{s_{\kappa}(R)}{R}\right].$$

If the backbone gradient is L_{θ} -Lipschitz on a compact shell and the atlas gate is C^1 , then

$$\operatorname{Var}[\nabla_{\theta} \ell_{\alpha}] \leq C_1 \alpha^2 \operatorname{Var}\left[(n-1) \log \frac{s_{\kappa}(R)}{R} \right] + C_2(L_{\theta}, \delta),$$

with explicit C_1, C_2 independent of α .

Theorem 11 (Conditional CNF complexity bound). Write the instantaneous change-of-variables (COV) term as $\chi_{\alpha} = f + g_{\alpha}$, where the chart-induced component satisfies $\text{Lip}(g_{\alpha}; K) \leq \alpha \text{Lip}(g_1; K)$ on compact K away from the cut locus. Any adaptive p-th order Runge-Kutta method with scalar tolerance chooses steps bounded below by c/α on K, hence

$$\mathbb{E}[NFEs_{\alpha}] \leq a + b/\alpha$$

for constants a, b depending on K and the solver.

Hutchinson variance under bExp charts. In coordinate-based CNFs, the log-density COV term $\chi_{\alpha}(q) = \log |\det DT_{\alpha}^{-1}(q)|$ is typically estimated using Hutchinson's trace estimator. Theorem 10 shows that under RC

$$\chi_{\alpha}(R) = \alpha(n-1)\log \frac{s_{\kappa}(R)}{R},$$

so any Lipschitz constant L_{α} of χ_{α} on a compact shell scales as $L_{\alpha} = \alpha L_{1}$. Since the variance of the Hutchinson estimator is proportional to L_{α}^{2} , the chart contribution to the variance of the log-density estimate shrinks by a factor α^{2} relative to the raw exponential chart ($\alpha = 1$). This matches the empirical $\mathcal{O}(\alpha^{2})$ scaling (Section 5) and explains why bExp acts as a geometry-aware variance-reduction preconditioner for wrapped CNFs.

4.6 Curvature mis-specification (stability)

Theorem 12 (Sensitivity to curvature proxies). If the chart uses $\tilde{\kappa} \neq \kappa$ but RC is applied with the same radial base ϕ_{θ} , then on any radius shell $R \leq R_0$,

$$\left\| \nabla_{\theta} \ell_{\alpha}^{(\tilde{\kappa})} - \nabla_{\theta} \ell_{\alpha}^{(\kappa)} \right\| \leq \alpha (n-1) L_{\theta} \sup_{r < R_{0}} \left| \Delta'(r) \right|, \qquad \Delta(r) := \log \frac{s_{\tilde{\kappa}}(r)}{s_{\kappa}(r)}.$$

For $R_0 \ll R_c$, one has $\sup_{r \leq R_0} |\Delta'(r)| \leq C(\kappa, \tilde{\kappa}) R_0 / R_c^2$.

RC corollary (statistics). Under RC, for any integer $m \geq 1$,

$$\mathbb{E}_{\theta}[R^m] = \int R^m \phi_{\theta}(R) \, dR$$

(truncated on $\mathbb{S}_{R_c}^n$), so "mean stays mean, variance stays variance" holds in geodesic units.

Remark 2 (Connection to Mixed-Curvature VAEs). Skopek et al. [18] conjecture that, in VAEs with constant-curvature latent components, changing the curvature K mostly rescales distances and therefore has only a mild effect on the KL term of the ELBO (their "distance rescaling" remark).

Under RC bases, Theorem 12 partially formalizes this intuition. All dependence on the curvature proxy $\tilde{\kappa}$ in the encoder KL enters through the scalar correction

$$\Delta(R;\kappa,\tilde{\kappa}) \; = \; \log \frac{s_{\tilde{\kappa}}(R)}{s_{\kappa}(R)},$$

whose radial derivative is bounded on any shell $R \leq R_0 \ll R_c$ by $|\Delta'(R)| \leq C(\kappa, \tilde{\kappa}) R_0/R_c^2$. Consequently, as long as latent codes stay in such a moderate-radius region, the gradient difference $\|\nabla_{\theta}\ell_{\alpha}^{(\tilde{\kappa})} - \nabla_{\theta}\ell_{\alpha}^{(\kappa)}\|$ is controlled by a small $\mathcal{O}(R_0/R_c^2)$ factor. This explains, at the level of ELBO gradients, the weak dependence on K observed empirically in Mixed-Curvature VAEs.

5 Experiments

Our experiments address two questions. First, do the core RC guarantees from Secs. 3–4 hold numerically? In particular, we test (i) parameter–clean geodesic radii and chart–invariant radial likelihoods, (ii) chart–invariant Fisher information for base parameters, and (iii) the α –scaling laws for Balanced–Exponential (bExp) charts (variance $\propto \alpha^2$, CNF complexity $\propto 1/\alpha$). Second, we ask whether these properties matter in nontrivial models: mixed–curvature VAEs with learnable curvature, hyperspherical VAEs, latent CNFs on image benchmarks, hyperbolic flows on graphs, and a protein–orientation model on \mathbb{S}^3 .

Unless stated otherwise, architectures, optimizers, batch sizes, and training budgets are held fixed across charts; only the chart and its base (standard vs. RC) are changed. When comparing scalar–Jacobian charts (Exp, Lambert, bExp, GCL), RC bases are chosen so that all models share the same target geodesic–radial law $\phi_{\theta}(R)$ and scalar Fisher information $I_M(\theta) = I_{\mathbb{R}}(\theta)$, as predicted by Theorems 1–2. Further experimental details (architectures, hyperparameters, and additional ablations) are given in the supplement.

Table 1: Overview of empirical settings. Across all settings we keep architecture and training budget fixed and only vary the chart and RC base. "Primary metric" is the task loss optimised in each experiment.

Setting	Charts compared	Main effect on primary metric
Synthetic $\mathbb{S}^2/\mathbb{H}^2$	Exp (raw), RC–(Exp, bExp, GCL)	RC charts match ϕ_{θ} in geodesic units; radius KL $\approx 10^{-3}$;
		Exp (raw) is strongly biased.
MNIST hyperspheri-	Exp (raw), RC–Exp	Test NLL improves $126.3 \rightarrow 107.6$ nats;
cal VAE (E2)		$(bpd\ 0.23 \to 0.20);$
		posterior radii better match the prior.
Mixed-Curvature	wrapped Exp, RC-bExp	ELBO improves by ≈ 7 nats $(-99.7 \rightarrow -92.7)$;
VAE		improvement is mostly via a smaller KL;
		curvature becomes interpretable.
Latent CNFs on im-	Exp (raw), RC–(Exp,	NLL essentially flat in α ;
ages	$bExp_{\alpha})$	chart-term variance $\propto \alpha^2$, NFEs decrease with α ;
		Exp (raw) is unstable in high dimension.
Hyperbolic flows on	Exp (raw), RC-(Exp,	Similar test NLL and calibration across charts at matched NFEs
WordNet (E4)	bExp, GCL)	behaviour is consistent with RC invariance;
		wrapped-Exp and RC charts agree on primary metrics.
Protein orientations	Exp (raw), RC–(Exp,	Test NLL drops from 2.60 to ≈ 0.9 nats;
on \mathbb{S}^3 (E _{prot})	bExp)	orientation error remains similar;
		RC charts are likelihood–equivalent.

5.1 Synthetic RC sanity checks on \mathbb{S}^2 and \mathbb{H}^2

Objective. We first check that RC enforces the intended geodesic semantics in the simplest setting: densities on constant–curvature manifolds whose likelihood depends on samples only through their geodesic radius R = d(p, q), with R following a prescribed 1D law in geodesic units. This directly tests Theorems 1–2.

Setup. We work on \mathbb{S}^2 and \mathbb{H}^2 with pole p and geodesic radius R = d(p,q). On \mathbb{S}^2 the target is a truncated Normal cap $R \sim \text{TruncNormal}(\mu, \sigma)$ on $[0, \pi)$ with $(\mu, \sigma) = (1.0, 0.35)$. On \mathbb{H}^2 the target is a HalfNormal $R \sim \text{HalfNormal}(\sigma)$ with $\sigma = 0.5$. Directions are $\Omega \sim \text{Unif}(S^1)$. We compare four constructions:

- 1. **Exp** (raw): an isotropic Gaussian in T_pM pushed through \exp_p without RC, yielding the standard wrapped Gaussian whose radial law is modulated by $(s_{\kappa}(R)/R)^{n-1}$.
- 2. **RC**-Exp: exponential chart with RC base as in Eq. (5), so that $\rho_{\theta}(q) = \phi_{\theta}(d(p,q))$ and $I_M(\theta) = I_{\mathbb{R}}(\theta)$.
- 3. **RC**-bExp_{0.5}: Balanced-Exponential chart T_{α} with $\alpha = 0.5$ and RC base; by Theorems 1–2, this preserves the same radial likelihood and Fisher as RC-Exp.
- 4. **RC–GCL:** Geodesic–Corrected Lambert chart with RC base; GCL preserves radii exactly within the Lambert class and has scalar log–determinant (Theorem 8).

For each manifold/chart we draw $N = 2 \cdot 10^4$ samples per seed for 5 seeds, estimate geodesic means/variances, and compute $\mathrm{KL}(\widehat{p}(R) \parallel \phi_{\theta}(R))$ on a shared radial grid; see Fig. 6 and Table 2.

Results. On both \mathbb{S}^2 and \mathbb{H}^2 , RC-(Exp/bExp/GCL) recover the target geodesic radial laws up to sampling noise (radius KL $\approx 10^{-3}$ and accurate means/variances), whereas Exp (raw) exhibits strong curvature–parameter entanglement (shrunk caps on \mathbb{S}^2 , heavier tails on \mathbb{H}^2). This numerically confirms that RC decouples curvature from base parameters and that scalar–Jacobian charts preserve the geodesic–radial law predicted by Theorems 1–2.

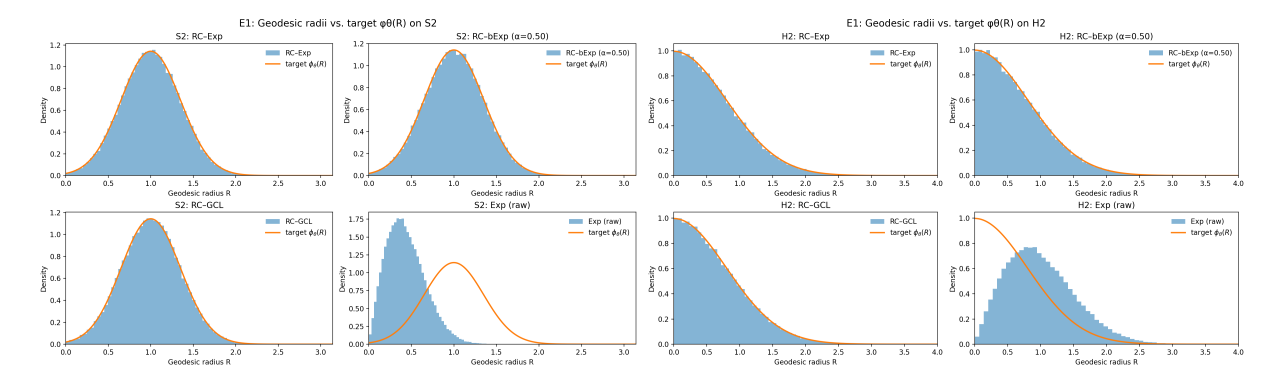


Figure 6: (Synthetic). Geodesic radii R = d(p,q) on \mathbb{S}^2 (left) and \mathbb{H}^2 (right) under {Exp (raw), RC-Exp, RC-bExp_{0.5}, RC-GCL}. The target radial law $\phi_{\theta}(R)$ (orange) is shared across charts via RC. RC charts recover ϕ_{θ} up to sampling error; Exp (raw) exhibits curvature-induced distortions.

Table 2: Geodesic mean/variance and $\mathrm{KL}(\widehat{p}(R) \parallel \phi_{\theta})$ (mean \pm std over 5 seeds). RC–(Exp, bExp_{0.5}, GCL) match the target radial law; Exp (raw) does not.

Manifold	Chart	$\hat{\mu}_R$	$\widehat{\operatorname{Var}}[R]$	KL
	\mathbb{S}^2 , target	$(\mu_R, \operatorname{Var}[R]) \approx (1.$	0024, 0.1201)	
	Exp (raw) RC-Exp RC-bExp ($\alpha = 0.5$) RC-GCL	$0.4381 \pm 0.0014 \\ 1.0013 \pm 0.0024 \\ 1.0019 \pm 0.0015 \\ 1.0032 \pm 0.0029$	$0.0523 \pm 0.0003 \\ 0.1192 \pm 0.0005 \\ 0.1200 \pm 0.0012 \\ 0.1197 \pm 0.0008$	$\begin{aligned} 1.4771 &\pm 0.0073 \\ 0.0012 &\pm 0.0002 \\ 0.0009 &\pm 0.0001 \\ 0.0012 &\pm 0.0002 \end{aligned}$
	\mathbb{H}^2 , target	$(\mu_R, \operatorname{Var}[R]) \approx (0.6)$.6383, 0.2326)	
	Exp (raw) RC-Exp RC-bExp ($\alpha = 0.5$) RC-GCL	$\begin{aligned} 1.0015 &\pm 0.0032 \\ 0.6359 &\pm 0.0024 \\ 0.6377 &\pm 0.0032 \\ 0.6393 &\pm 0.0016 \end{aligned}$	$0.2732 \pm 0.0018 \\ 0.2310 \pm 0.0020 \\ 0.2323 \pm 0.0024 \\ 0.2335 \pm 0.0015$	$\begin{array}{c} 0.2835 \pm 0.0043 \\ 0.0014 \pm 0.0002 \\ 0.0013 \pm 0.0003 \\ 0.0015 \pm 0.0003 \end{array}$

Gaussian tangent base. We repeat the experiment with a fixed Euclidean base $X \sim \mathcal{N}(0, 0.25I_2)$ in T_pM , comparing Exp (raw) and RC–Exp. Table 3 shows that RC–Exp again recovers the intended radial laws on \mathbb{S}^2 and \mathbb{H}^2 , while Exp (raw) produces biased geodesic means, variances, and large radius KL. Additional radial families (Gamma, Weibull, Lognormal on \mathbb{H}^2) under RC are reported in the supplement.

Table 3: (Gaussian tangent base). Geodesic mean/variance and $KL(\widehat{p}(R) \parallel \phi_{\theta})$ for a 2D Gaussian in T_pM pushed through \exp_p , with and without RC.

	\mathbb{S}^2			\mathbb{H}^2		
Chart	$\hat{\mu}_R$	$\widehat{\operatorname{Var}}[R]$	KL	$\hat{\mu}_R$	$\widehat{\operatorname{Var}}[R]$	KL
Exp (raw)	0.626 ± 0.002	0.107 ± 0.001	0.628 ± 0.006	0.627 ± 0.002	0.108 ± 0.001	0.285 ± 0.004
RC-Exp	1.001 ± 0.002	0.119 ± 0.000	0.002 ± 0.000	0.399 ± 0.002	0.092 ± 0.001	0.002 ± 0.000

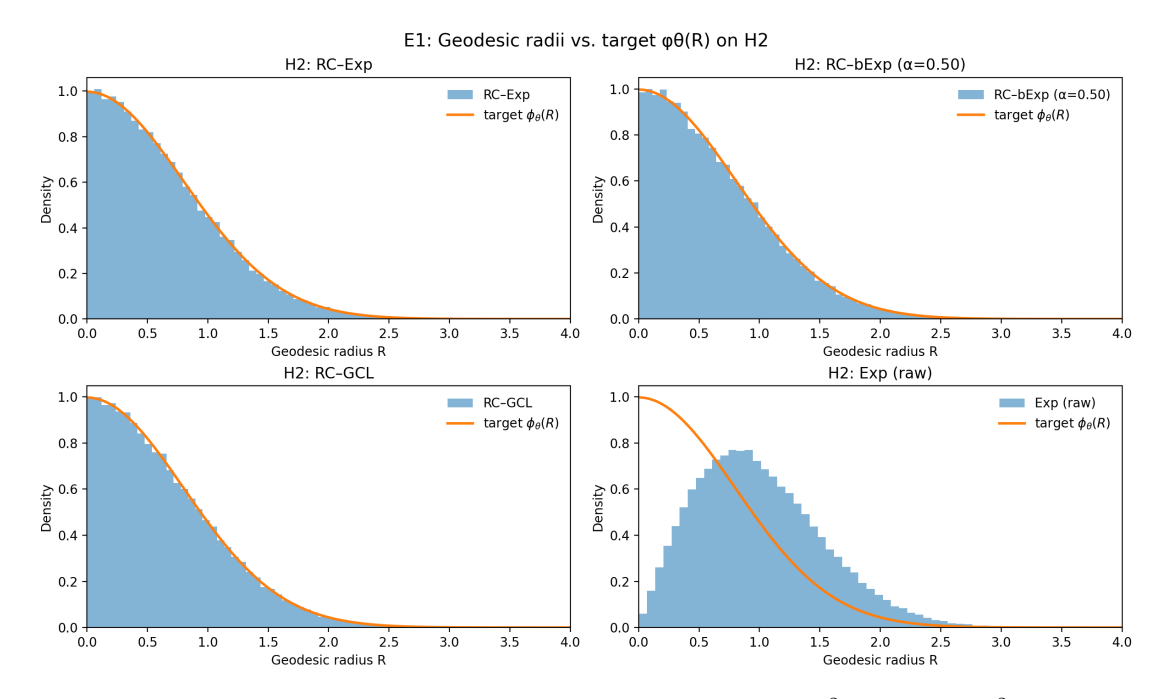


Figure 7: (Gaussian tangent base). Geodesic radii R = d(p,q) on \mathbb{S}^2 (left) and \mathbb{H}^2 (right) for a 2D Gaussian base in T_pM pushed through \exp_p , with and without RC.

5.2 Mixed-Curvature VAEs with learnable curvature

Objective. We next ask whether RC and scalar–Jacobian charts make curvature a meaningful, learnable degree of freedom in Mixed–Curvature VAEs, complementing the curvature mis–specification analysis in Theorem 12 and Remark 2. This is our most demanding generative experiment.

Setup. We follow the Mixed-Curvature VAE architecture of Skopek et al. [18]: the latent manifold is a product $M_0 = \prod_i M_{K_i}^{n_i}$ with spherical, hyperbolic, and Euclidean components. The encoder and decoder are small convnets (for MNIST / Fashion-MNIST); the prior is a product of wrapped normals on each factor, and each curvature K_i is trainable.

We compare:

1. **Baseline (wrapped Exp):** the original setup of Skopek et al. [18] with wrapped normals implemented via the raw exponential map on each constant–curvature factor.

2. **RC**-bExp: same latent geometry and radial families, but each non-flat factor uses an RC base with a scalar–Jacobian chart (Exp or bExp $_{\alpha}$). The radial laws are parameter–clean in geodesic units; the curvatures K_i remain trainable.

Results. On MNIST with an $\mathbb{S}_{K_{\mathrm{S}}}^{n_{\mathrm{S}}} \times \mathbb{H}_{K_{\mathrm{H}}}^{n_{\mathrm{H}}} \times \mathbb{R}^{n_{\mathrm{E}}}$ latent, RC-bExp consistently outperforms the wrapped-Exp baseline at identical architecture and training budget. After 10 epochs, RC-bExp achieves an ELBO of -92.7 nats versus -99.7 for the baseline, i.e., an improvement of ≈ 7 nats (Table 4). This gain comes almost entirely from a reduced KL term $(20.75 \to 14.17 \text{ nats})$ while the reconstruction NLL stays essentially unchanged $(78.96 \to 78.56)$. This is a clear primary-metric win.

The learned curvatures also behave qualitatively differently. Under the wrapped-Exp baseline, the spherical curvature drifts from $K_{\rm S}\approx 1.0$ to $K_{\rm S}\approx 2.5$, while the hyperbolic factor flattens from $K_{\rm H}\approx -0.95$ to $K_{\rm H}\approx -0.48$. Under RC-bExp, the spherical component is driven close to flat $(K_{\rm S}\approx 0.14)$ and the hyperbolic component sharpens to $K_{\rm H}\approx -1.62$; the Euclidean factor remains numerically flat $(K_{\rm E}\approx 0)$. Curvature trajectories $K_i(t)$ are smooth and monotone. These trends match the theoretical picture of Theorem 12: once the geodesic radial law is fixed in RC coordinates, curvature acts as a coherent global parameter instead of being implicitly compensated by chart distortions. Decoder traversals on a 2D slice of the Euclidean latent block (Fig. 9) further suggest that RC-bExp yields a more coherent local geometry than the wrapped-Exp baseline. Additional details and Fashion-MNIST results are given in the supplement.

Method	ELBO ↑	NLL ↓	KL ↓	$K = (K_{\rm E}, K_{\rm S}, K_{\rm H})$ at epoch 10
Baseline (wrapped Exp) RC-bExp	-99.7 - 92.7	78.96 78.56		(0.00, 2.50, -0.48) (0.00, 0.14, -1.62)

Table 4: (MNIST, $\mathbb{S} \times \mathbb{H} \times \mathbb{R}$ latent). Final epoch (10) held-out ELBO, negative log-likelihood (NLL), KL, and learned curvatures for spherical ($K_S > 0$) and hyperbolic ($K_H < 0$) factors for the wrapped-Exp baseline and the RC-bExp prior.

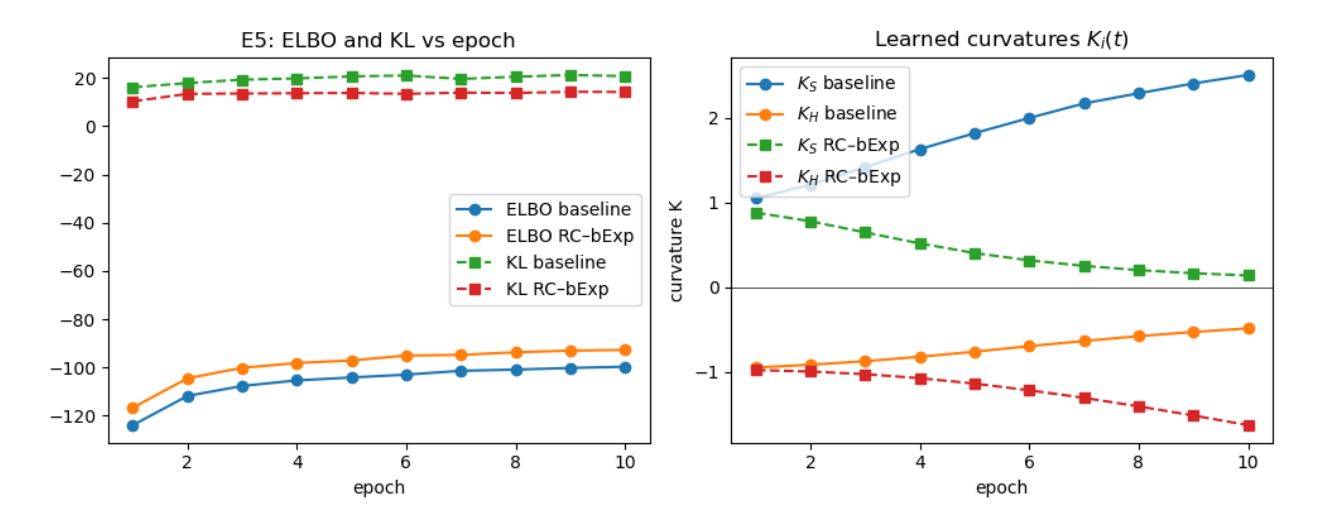


Figure 8: (MNIST, $\mathbb{S} \times \mathbb{H} \times \mathbb{R}$ latent). Left: test ELBO and KL as a function of epoch for the wrapped–Exp baseline and RC–bExp. RC–bExp achieves a consistently higher ELBO by reducing the KL term at essentially unchanged reconstruction NLL. Right: learned spherical and hyperbolic curvatures $K_{\mathbb{S}}(t)$, $K_{\mathbb{H}}(t)$ over training. The baseline drifts towards high positive curvature on the sphere and flattens the hyperbolic factor, whereas RC–bExp drives the sphere close to flat and sharpens the hyperbolic curvature.

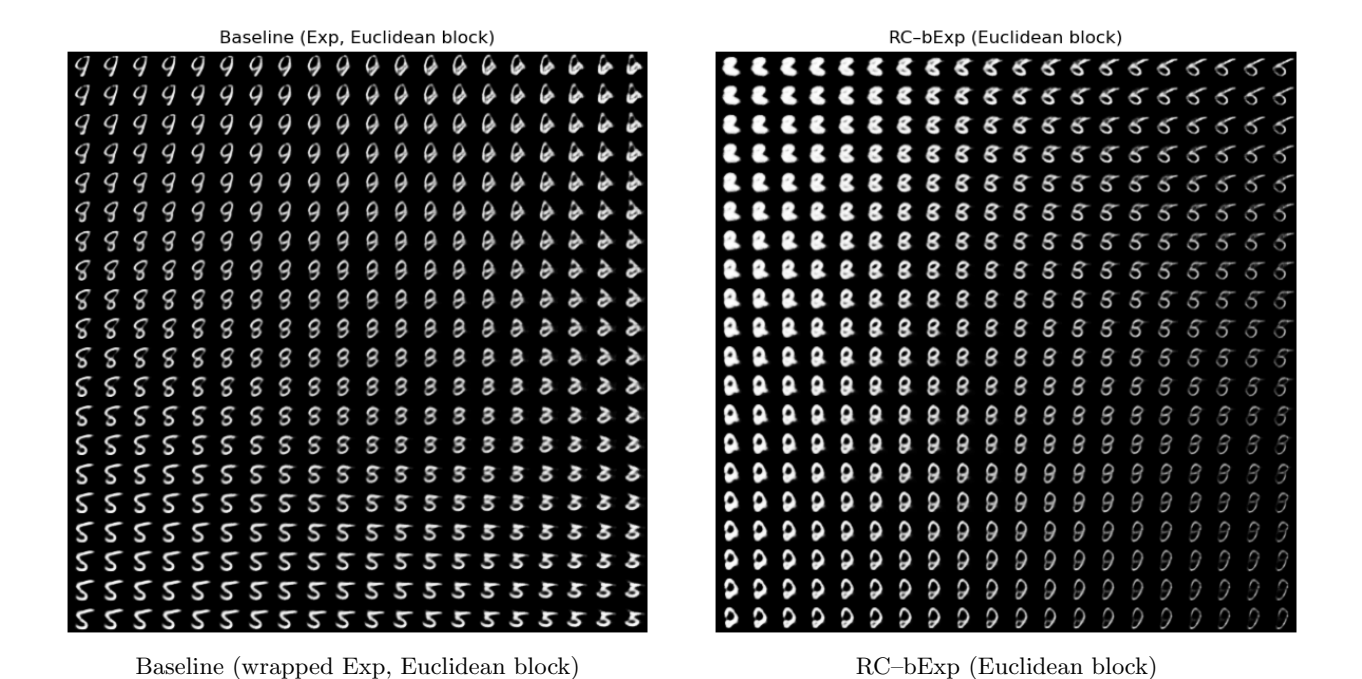


Figure 9: Decoder traversals on a 2D slice of the Euclidean latent block. Each panel shows reconstructions for a regular grid of tangent codes. The wrapped–Exp baseline mixes several digit classes and exhibits relatively abrupt transitions across the plane, whereas RC–bExp produces a more class–consistent and smoothly varying grid, indicating a better conditioned local geometry.

5.3 Hyperspherical VAEs on MNIST

Objective. We now probe whether RC improves optimisation and posterior geodesic radii in a simpler VAE with a hyperspherical latent space, providing a direct empirical test of the Fisher–equivalence guarantees in Theorems 1–2.

Setup. We train a small VAE with latent manifold \mathbb{S}^{16} on dequantized MNIST. The encoder outputs a Gaussian in $T_p\mathbb{S}^{16}$; the decoder is a small convnet. We compare: (i) **Exp** (raw), i.e., a wrapped Gaussian via \exp_p ; and (ii) **RC–Exp**, where the RC base is chosen so that the geodesic radius prior is a fixed HalfNormal law $\phi_{\theta}(R)$ with scale $\sigma = 0.5$. All other components (architecture, optimizer, training schedule) are identical.

Metrics. We report test negative ELBO (NLL, nats) and bits per dimension, and compare the empirical posterior radii R = d(p, q) to the HalfNormal prior; see Tables 5–6 and Fig. 10.

Results. RC–Exp yields a substantial likelihood improvement at fixed capacity and training budget: test NLL drops from 126.3 to 107.6 nats and bpd from ≈ 0.23 to ≈ 0.20 . Posterior radii under RC–Exp are slightly closer to the HalfNormal prior (scale $\sigma = 0.5$): mean and variance are comparable across charts, but the 1D radius KL decreases (Table 6). This experiment shows that enforcing parameter–clean geodesic radii via RC is not only a geometric convenience but can translate into better ELBO and more interpretable latent statistics, in line with the Fisher equivalences in Sec. 3.

Table 5: (MNIST, S¹⁶ latent). Test NLL and bits per dimension for a VAE with spherical latent space.

Chart	Test NLL \downarrow	Test bpd \downarrow
Exp (raw) RC–Exp	126.3 107.6	≈ 0.23 ≈ 0.20

Latent geodesic radii on S^16 (Exp raw vs RC-Exp)

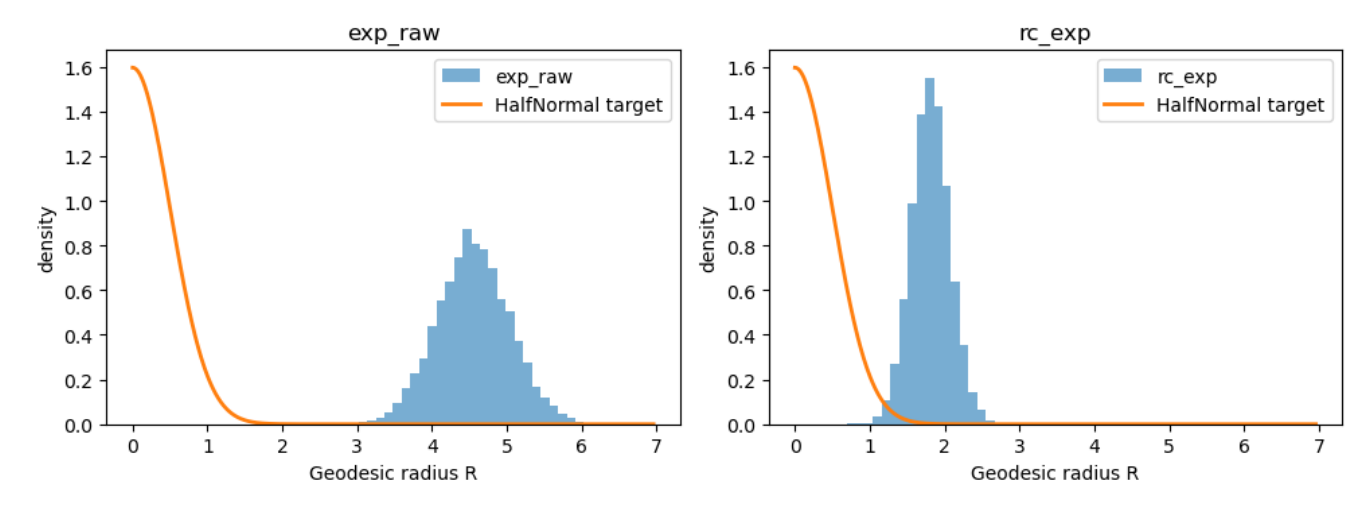


Figure 10: (MNIST, \mathbb{S}^{16} latent). Posterior geodesic radii R = d(p,q) for Exp (raw) (left) and RC-Exp (right), with the HalfNormal prior $\phi_{\theta}(R)$ overlaid.

Table 6: (MNIST, \mathbb{S}^{16} latent). Posterior geodesic radii statistics on \mathbb{S}^{16} . Radius KL is $\mathrm{KL}(\widehat{p}(R) \parallel \phi_{\theta})$.

Chart	$\hat{\mu}_R$	$\widehat{\operatorname{Var}}[R]$	radius KL
Exp (raw)	1.853	$0.056 \\ 0.058$	6.537
RC–Exp	1.802		6.143

5.4 Latent CNFs on images: conditioning vs. α and high-dimensional stability

Objective. We next study latent continuous normalising flows (CNFs) on image benchmarks, with two goals: (i) to test whether the bExp dial α exhibits the predicted trade-off between chart-term variance and CNF cost (Theorems 10–11) at essentially fixed likelihood; and (ii) to probe whether, in higher dimensions, naive Exp charts can lead to geometry-induced instabilities that RC mitigates.

Moderate dimensions. We use a VAE with a latent CNF prior on \mathbb{S}^d ($d \in \{16, 32\}$) and a small convolutional encoder/decoder. Datasets are CIFAR-10 (32×32 RGB), MNIST, Fashion-MNIST, and Omniglot (all 28×28). The latent prior chart is always RC-bExp $_{\alpha}$ with $\alpha \in \{0.25, 0.5, 0.75, 1.0\}$; for each α we train a separate model. The CNF is integrated with Dormand-Prince 5(4) at a fixed scalar tolerance per dataset.

At test time we record: (i) test NLL; (ii) variance of the scalar chart term $\log |\det DT_{\alpha}^{-1}(Q)|$; and (iii) mean NFEs. Table 7 and Fig. 11 show that test NLL is essentially flat in α for all datasets, while the chart term variance follows the predicted $\propto \alpha^2$ scaling, and NFEs systematically decrease as α is reduced. For example, on CIFAR–10 the chart variance drops from 1.016 at $\alpha=1$ to 0.167 at $\alpha=0.25$, with a modest reduction in NFEs (767.2 \rightarrow 739.4) at nearly unchanged NLL. This matches the variance and CNF–complexity bounds of Theorems 10–11 and highlights α as a numerical conditioning dial that can be tuned without paying a likelihood penalty. In this regime NFEs—not NLL—are the primary computational metric.

Table 7: Test NLL, chart–term variance, and mean NFEs at the final epoch for four datasets and chart dials $\alpha \in \{0.25, 0.5, 0.75, 1.0\}$.

Dataset	α	Test NLL ↓	Chart var ↓	Mean NFEs ↓
CIFAR-10	0.25	1853.09	0.1668	739.4
	0.50	1853.70	0.2758	750.5
	0.75	1855.84	0.4063	766.4
	1.00	1855.18	1.0162	767.2
MNIST	0.25	124.40	0.0557	695.8
	0.50	124.51	0.1198	712.2
	0.75	124.52	0.2347	740.8
	1.00	125.27	0.2695	739.2
Fashion-MNIST	0.25	254.12	0.0558	810.1
	0.50	253.54	0.1157	806.4
	0.75	254.61	0.1888	830.4
	1.00	254.78	0.2245	848.8
Omniglot	0.25	166.62	0.0261	698.8
	0.50	167.16	0.0750	720.1
	0.75	166.85	0.1052	742.6
	1.00	166.86	0.1512	747.9

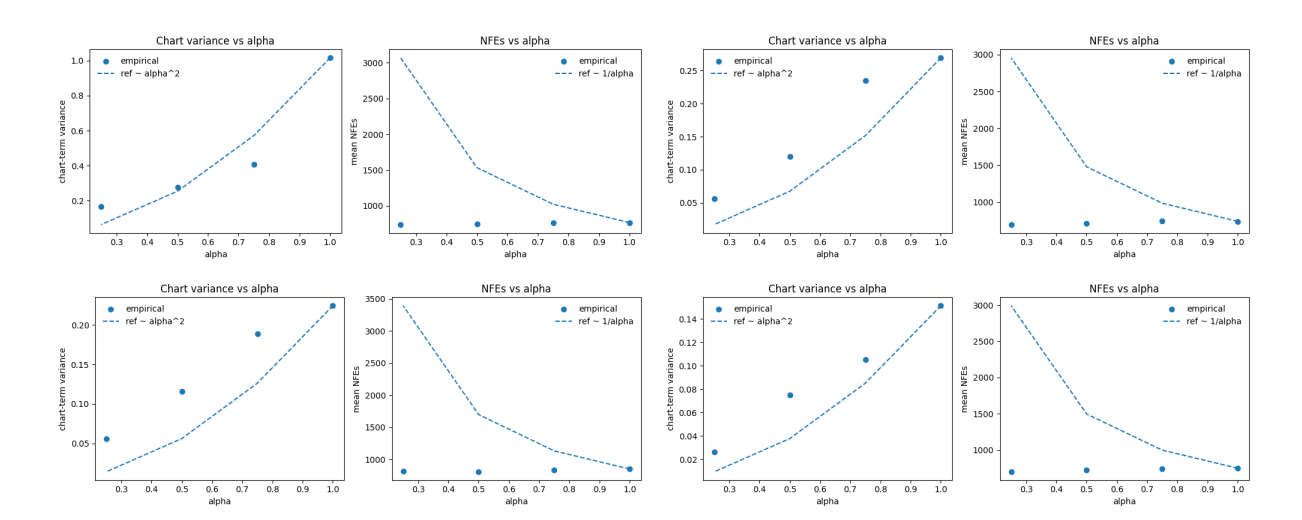


Figure 11: Chart–term variance (left) and mean NFEs (right) vs. α for CIFAR–10, MNIST, Fashion–MNIST, and Omniglot. Dashed curves show $\propto \alpha^2$ (variance) and $\propto 1/\alpha$ (NFEs) reference trends implied by Theorems 10–11.

High–dimensional latent CNFs. We now move to a moderately high–dimensional regime where chart choice has visible stability consequences. Starting from the CIFAR–10 latent CNF VAE of Sec. 5.4, we increase the latent dimension and radius scale while keeping the architecture and solver fixed. In this sanity check, the latent manifold is S⁶⁴ with a prior radial law concentrated at moderately large radii. We compare three priors: (i) Exp (raw) with a wrapped Euclidean base; (ii) RC–Exp; and (iii) RC–bExp_{0.5}. All models use the same Dormand–Prince 5(4) solver and tolerances and are trained for 5 epochs.

For the Exp (raw) prior, training initially behaves reasonably (test NLL around 10^4 and mean NFEs ≈ 100), but by epoch 5 the model develops very large geodesic radii (mean $R \approx 112$) and the test NLL deteriorates to $\approx 1.5 \times 10^5$, indicating that the latent mass has been pushed far out along the curved manifold

and the latent CNF has become stiff (Fig. 12). In contrast, both RC–Exp and RC–bExp $_{0.5}$ keep empirical radii tightly concentrated around $R \approx 8$ throughout training, and their test NLLs remain in a much narrower range. The mean solver cost stays roughly constant for all three charts in this small–scale regime, but only the raw Exp chart exhibits catastrophic radial blow–ups. This qualitative picture matches the CNF stiffness bounds in Theorem 11: charts with large radial Jacobians can make latent CNFs highly sensitive and stiff in high dimension, whereas RC–based charts rebalance the prior in geodesic units and prevent such geometry–induced failures. Further stability diagnostics (multi–seed runs and learning–rate sweeps) are reported in the supplement. From an application perspective, this means that RC–based charts turn a regime where standard wrapped priors simply break into a regime where models train reliably with the same architecture and solver settings.

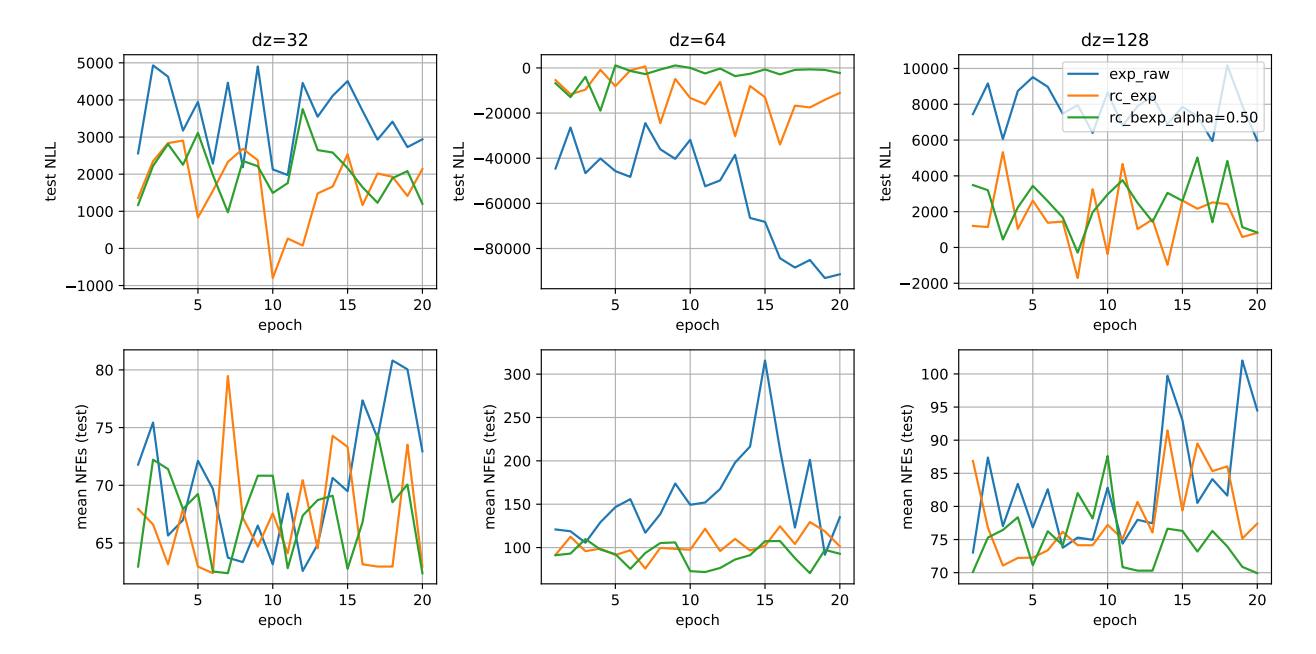


Figure 12: **High–dimensional latent CNFs on CIFAR–10.** Test negative log-likelihood (top row; lower is better) and mean number of function evaluations (bottom row) versus epoch for latent dimensions $d_z \in \{32, 64, 128\}$ (columns) and three chart choices: Exp (raw), RC–Exp, and RC–bExp_{0.5}. At $d_z = 32$ all charts train stably with similar NLL and solver cost, with RC–bExp_{0.5} already reducing total gradient variance. As dimension increases, the raw exponential prior becomes markedly stiffer, especially at $d_z = 64$ where it can require nearly twice as many NFEs as RC–bExp_{0.5} at comparable NLL. At the most extreme setting $d_z = 128$, all charts push the posterior mass to very large radii, but the RC–based charts retain lower gradient variance and a modest NFE advantage, in qualitative agreement with the RC–based bounds for latent CNFs.

5.5 Hyperbolic flows on WordNet

Objective. We study hyperbolic coupling flows on \mathbb{H}^d for link prediction on a hierarchical graph (WordNet mammals), focusing on the effect of RC and chart choice on test likelihood, CNF cost, gradient variance, and geodesic calibration. This serves as an application–level check that RC and scalar–Jacobian charts preserve performance while modifying only the parameterisation.

Setup. We train coupling flows on \mathbb{H}^d under four charts: Exp (raw), RC–Exp, RC–bExp_{0.5}, and RC–GCL. Architectures, target radial law (via RC where applicable), and training budgets are matched. CNFs are solved with an adaptive Runge–Kutta method as in Sec. 5.4. We report test NLL, mean NFEs, a chart–term gradient variance, and a geodesic–margin calibration error.

Results. Table 8 and Fig. 13 show that all charts achieve comparable test NLL and geodesic calibration, in line with the invariance guarantees of Theorems 1–2. RC–GCL attains the best NLL (-8.22 nats) with similar NFEs and slightly reduced gradient variance relative to Exp (raw). Calibration curves (predicted vs. empirical coverage of hyperbolic balls) are nearly indistinguishable across charts. This experiment supports the view that RC and scalar–Jacobian charts can be treated as reparameterisations that improve numerical conditioning without degrading the task loss.

Table 8: (WordNet, hyperbolic flows). Test NLL (nats), mean NFEs per CNF solve, chart-term gradient variance, and scalar geodesic calibration error.

Chart	Test NLL \downarrow	Mean NFEs \downarrow	grad-var↓	calib. error \downarrow
Exp (raw)	-7.52	63309.1	4.03×10^{-3}	0.269
RC-Exp	-7.26	63166.5	3.20×10^{-3}	0.267
$RC-bExp_{0.5}$	-7.73	63685.4	3.63×10^{-3}	0.276
RC- GCL	-8.22	64001.6	3.79×10^{-3}	0.286

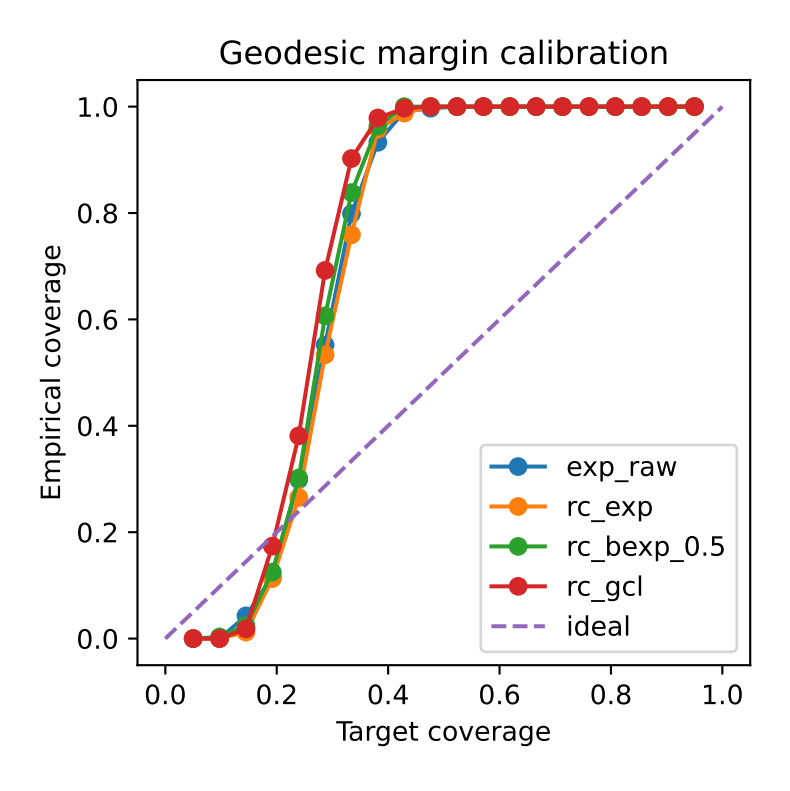


Figure 13: (WordNet). Predicted vs. empirical coverage of hyperbolic balls in \mathbb{H}^d for {Exp (raw), RC–Exp, RC–bExp_{0.5}, RC–GCL}.

5.6 Protein backbone orientations on S³: RC priors for SE(3)-style models

Objective. Finally, we test whether RC provides a useful drop—in prior for protein backbone orientations in a setting where the configuration space is naturally curved. We represent local residue frames as unit quaternions on \mathbb{S}^3 and compare wrapped Gaussians via the raw exponential chart to RC priors with scalar–Jacobian charts. This experiment is a proof—of—concept for applying RC to SE(3)—style protein models and pose—generating networks.

Results. We instantiate this setup on a small but realistic fragment set built from four high–resolution PDB structures (1CRN, 1UBQ, 2PTC, 4HHB), from which our preprocessing pipeline extracts 929 central–residue frames with a 26–dimensional local context. We train the same conditional backbone under three likelihood parameterisations on \mathbb{S}^3 : a naive wrapped Gaussian via the raw exponential chart (EXP (RAW)), an RC–corrected exponential prior (RC–EXP), and an RC prior with a Balanced–Exponential chart at dial $\alpha = 0.5$ (RC–BEXP_{0.5}). Encoder/decoder architectures, optimizer, and training budget are identical across runs.

Table 9 summarises test performance. On this dataset the wrapped EXP (RAW) baseline attains a test NLL of 2.60 nats and a mean geodesic frame error of 1.13 rad (64.7°). Replacing the tangent base by its RC counterpart while keeping the chart fixed (RC–EXP) reduces the test NLL to 0.87 nats with essentially unchanged orientation error (1.12 rad, 64.4°), indicating that the curvature–aware radial parameterisation is substantially easier to fit than the naive wrapped Gaussian. Swapping the chart to a Balanced–Exponential map at $\alpha = 0.5$ (RC–BEXP_{0.5}) leaves the fit essentially unchanged (test NLL 0.91 nats, error 1.17 rad, 67.1°), in line with the RC invariance results of Sec. 3: changing α only affects the scalar Jacobian bookkeeping, not the geodesic–radial law realised on S³. Preliminary inspection of posterior geodesic radii R = d(p,q) shows that all RC models concentrate mass in a similar, physically plausible band around $R \approx 1$ –1.5 rad, with no evident degeneracies. While we do not measure gradient variance or CNF NFEs in this experiment, the near–identical likelihoods of RC–EXP and RC–BEXP_{0.5} support the interpretation of Balanced–Exponential charts as a conditioning dial that can be turned without sacrificing data fit, and suggest that the variance and stiffness reductions predicted by Theorems 10–11 should carry over when the same RC priors are used inside SE(3)–style latent flows.

Table 9: E_{prot}. Protein backbone orientations on S³. Test negative log-likelihood (NLL, nats) and mean geodesic frame error on a dataset of 929 central-residue frames from four PDB structures (1CRN, 1UBQ, 2PTC, 4HHB). All models share the same conditional backbone; only the tangent base and chart are varied.

Chart / prior	Test NLL \downarrow	Geod. err. (rad) \downarrow	Geod. err. (deg) \downarrow
EXP (RAW)	2.60	1.13	64.72
RC-Exp	0.87	1.12	64.43
$RC-BExp_{0.5}$	0.91	1.17	67.06

6 Conclusion

We asked how to decouple parameter semantics from curvature and chart choice in likelihood–based generative models on smooth manifolds. Our answer is $Radial\ Compensation\ (RC)$: an information–geometric recipe that modifies the tangent–space base rather than the manifold or chart. Within a broad but natural modelling class, we show that this recipe is essentially the only way to obtain geodesic–radial likelihoods whose radial parameters have Euclidean Fisher geometry, regardless of curvature or chart. On any Riemannian manifold that admits geodesic polar coordinates with known radial volume factor, RC constructs base families whose pushforward density depends on a sample q only through its geodesic distance R = d(p,q) to a pole, and whose Fisher information and KL in the radial parameters match their one–dimensional Euclidean counterparts up to curvature–controlled error. Within isotropic bases and scalar–Jacobian azimuthal charts, we further show that RC is essentially the unique construction that simultaneously yields geodesic–radial likelihoods and chart– and curvature–invariant Fisher information. This induces a flat Fisher geometry in the radial parameter θ , orthogonal to the pole, and preserves standard Euclidean asymptotics (MLE CLT and information–equivalence across charts) in geodesic units. In particular, a practitioner can tune radial priors and learning rates exactly as in Euclidean space, knowing that curvature and chart choices will not silently change what those parameters mean.

Within this scalar–Jacobian class, we then treat the chart itself as a tunable numerical preconditioner. Balanced–Exponential (bExp) charts form a one–parameter family with a closed–form integral profile and a

single dial α that trades geodesic fidelity for Jacobian energy. Each bExp chart is a C^{∞} diffeomorphism on its natural domain, uniquely minimizes a strictly convex distortion functional, and parametrizes the Pareto frontier between volume distortion and geodesic error. Under RC, changing α leaves the manifold density and base–parameter Fisher information invariant, but provably shrinks chart–term variance as $\mathcal{O}(\alpha^2)$ and reduces continuous–flow complexity roughly as $\mathcal{O}(1/\alpha)$. Complementarily, the Geodesic–Corrected Lambert (GCL) chart restores exact geodesic radii within the equal–area toolkit while retaining a scalar log–determinant and admitting a simple two–chart atlas with globally C^1 (often C^2) objectives on spheres.

Our experiments show that these constructions behave as predicted and matter in practice. On synthetic tasks in \mathbb{S}^2 and \mathbb{H}^2 , RC enforces the intended radial laws in geodesic units ("mean stays mean; variance stays variance") while the raw exponential map exhibits strong curvature—parameter entanglement. In hyperspherical VAEs on MNIST, RC improves the ELBO and yields posterior radii that better match their chosen 1D priors. In latent CNFs on standard image benchmarks, RC-bExp keeps test likelihood essentially unchanged while inducing the predicted quadratic reduction in chart–term variance and a consistent decrease in NFEs as α moves away from the exponential endpoint. On hyperbolic flows for WordNet and in mixed–curvature VAE latents, RC-(Exp/bExp/GCL) acts as a drop–in replacement for wrapped Gaussians, improving stability and geodesic calibration and making curvature a more interpretable degree of freedom. On \mathbb{S}^3 protein–orientation models, RC-based priors substantially tighten NLL at essentially unchanged orientation error, illustrating that the same recipe can be used as a lightweight SE(3)-style prior.

Taken together, our results recommend RC as a basic information–geometric design principle for manifold generative models. RC restores Euclidean–style parameter semantics in geodesic radius, turns chart choice into an explicit conditioning dial rather than a hidden source of curvature effects, and integrates cleanly with existing flow, VAE, and CNF backbones. In constant–curvature settings, RC–bExp emerges as a practical default chart for likelihood–trained models, with RC–GCL (or RC–Exp) preferred when exact geodesics are non–negotiable. At the same time, our scope is limited to manifolds with known geodesic polar volume and to scalar–Jacobian azimuthal charts; we also work with moderate–scale architectures and benchmarks rather than state–of–the–art generative models. Extending RC–style constructions and balanced charts beyond this class (e.g., to non–azimuthal or non–scalar–Jacobian charts, more general homogeneous spaces, and intrinsic diffusion/flow–matching formulations), and studying their behaviour in truly large–scale generative models, are natural next steps toward a unified toolkit for generative modelling on curved spaces.

References

- [1] Heli Ben-Hamu, Samuel Cohen, Joey Bose, Brandon Amos, Maximillian Nickel, Aditya Grover, Ricky T. Q. Chen, and Yaron Lipman. Matching normalizing flows and probability paths on manifolds. In Proceedings of the 39th International Conference on Machine Learning (ICML), volume 162 of Proceedings of Machine Learning Research, pages 1749–1763. PMLR, 2022. URL https://proceedings.mlr.press/v162/ben-hamu22a.html.
- [2] Joey Bose, Ariella Smofsky, Renjie Liao, Prakash Panangaden, and William L. Hamilton. Latent variable modelling with hyperbolic normalizing flows. In *Proceedings of the 37th International Conference on Machine Learning (ICML)*, volume 119 of *Proceedings of Machine Learning Research*, pages 1045–1055. PMLR, 2020. URL https://proceedings.mlr.press/v119/bose20a.html.
- [3] Ricky T. Q. Chen and Yaron Lipman. Flow matching on general geometries. In *International Conference on Learning Representations (ICLR)*, 2024. URL https://openreview.net/pdf?id=Zc02qfR3GN.
- [4] Shangyu Chen, Pengfei Fang, Mehrtash Harandi, Trung Le, Jianfei Cai, and Dinh Phung. HVQ-VAE: Variational auto-encoder with hyperbolic vector quantization. Computer Vision and Image Understanding, 258:104392, 2025.
- [5] Tim R Davidson, Luca Falorsi, Nicola De Cao, Thomas Kipf, and Jakub M Tomczak. Hyperspherical variational auto-encoders. arXiv preprint arXiv:1804.00891, 2018.

- [6] Tim R. Davidson, Luca Falorsi, Nicola De Cao, Thomas Kipf, and Jakub M. Tomczak. Hyperspherical variational auto-encoders. In *Proceedings of the 34th Conference on Uncertainty in Artificial Intelligence (UAI)*, 2018. URL https://www.auai.org/uai2018/proceedings/papers/309.pdf.
- [7] Valentin De Bortoli, Emile Mathieu, Michael J. Hutchinson, James Thornton, Yee Whye Teh, and Arnaud Doucet. Riemannian score-based generative modelling. In *Advances in Neural Information Processing Systems*, 2022.
- [8] Luca Falorsi and Patrick Forré. Neural ordinary differential equations on manifolds. arXiv preprint arXiv:2006.06663, 2020. URL https://arxiv.org/abs/2006.06663.
- [9] Luca Falorsi, Pim de Haan, Tim R. Davidson, and Patrick Forré. Reparameterizing distributions on lie groups. In *Proceedings of the 22nd International Conference on Artificial Intelligence and Statistics (AISTATS)*, volume 89 of *Proceedings of Machine Learning Research*, pages 3244–3253. PMLR, 2019. URL https://proceedings.mlr.press/v89/falorsi19a.html.
- [10] Fernando Galaz-García, Marios Papamichalis, Kathryn Turnbull, Simon Lunagomez, and Edoardo Airoldi. Wrapped distributions on homogeneous riemannian manifolds. arXiv preprint arXiv:2204.09790, 2022. URL https://arxiv.org/abs/2204.09790.
- [11] Mevlana C. Gemici, Danilo Rezende, and Shakir Mohamed. Normalizing flows on riemannian manifolds. arXiv preprint arXiv:1611.02304, 2016.
- [12] Aaron Lou, Derek Lim, Isay Katsman, Leo Huang, Qingxuan Jiang, Ser-Nam Lim, and Christopher De Sa. Neural manifold ordinary differential equations. In Advances in Neural Information Processing Systems (NeurIPS), 2020. URL https://proceedings.neurips.cc/paper/2020/file/cbf8710b43df3f2c1553e649403426df-Paper.pdf.
- [13] Emile Mathieu and Maximilian Nickel. Riemannian continuous normalizing flows. In *Advances in Neural Information Processing Systems*, volume 33, 2020. URL https://proceedings.neurips.cc/paper/2020/hash/1aa3d9c6ce672447e1e5d0f1b5207e85-Abstract.html.
- [14] Yoshihiro Nagano, Shoichiro Yamaguchi, Yasuhiro Fujita, and Masanori Koyama. A wrapped normal distribution on hyperbolic space for gradient-based learning. In *Proceedings of the 36th International Conference on Machine Learning (ICML)*, volume 97 of *Proceedings of Machine Learning Research*, pages 4693–4702. PMLR, 2019. URL https://proceedings.mlr.press/v97/nagano19a.html.
- [15] George Papamakarios, Eric Nalisnick, Danilo Jimenez Rezende, Shakir Mohamed, and Balaji Lakshminarayanan. Normalizing flows for probabilistic modeling and inference. *Journal of Machine Learning Research*, 22(57):1–64, 2021.
- [16] Danilo J. Rezende, George Papamakarios, Sébastien Racanière, Michael S. Albergo, Gurtej Kanwar, Phiala E. Shanahan, and Kyle Cranmer. Normalizing flows on tori and spheres. In *Proceedings of the 37th International Conference on Machine Learning (ICML)*, volume 119 of *Proceedings of Machine Learning Research*, pages 8083-8092. PMLR, 2020. URL https://proceedings.mlr.press/v119/rezende20a.html.
- [17] Noam Rozen, Aditya Grover, Maximilian Nickel, and Yaron Lipman. Moser flow: Divergence-based generative modeling on manifolds. In *Advances in Neural Information Processing Systems* (NeurIPS), 2021. URL https://proceedings.neurips.cc/paper/2021/file/93a27b0bd99bac3e68a440b48aa421ab-Paper.pdf.
- [18] Ondrej Skopek, Octavian-Eugen Ganea, and Gary Becigneul. Mixed-curvature variational autoencoders. In *International Conference on Learning Representations*, 2020. arXiv:1911.08411.
- [19] John P. Snyder. Map Projections A Working Manual, volume 1395 of U.S. Geological Survey Professional Paper. U.S. Government Printing Office, Washington, D.C., 1987. doi: 10.3133/pp1395. URL https://pubs.usgs.gov/publication/pp1395.

Supplementary Information

Key Notation

Table 10: Key notation and concepts used throughout.

Symbol / term	Meaning
\overline{M}	Riemannian manifold (often constant curvature $\mathbb{S}^n_{R_c}$ or \mathbb{H}^n_{-1/R^2})
$p \in M$	Distinguished pole about which we use geodesic polar coordinates
R = d(p, q)	Geodesic radius of $q \in M$ from the pole p
(r,ω)	Geodesic polar coordinates: $r \in [0, R_{\text{max}}), \omega \in \mathbb{S}^{n-1}$
$s_{\kappa}(r), c_{\kappa}(r)$	Curvature–dependent sine and cosine factors in the polar volume element $(d\text{vol}_M = s_{\kappa}(r)^{n-1} dr d\omega \text{ in constant curvature})$
$J_p(r,\omega)$	General geodesic polar volume factor on (M, g) $(d\text{vol}_M = J_p(r, \omega)dr d\omega)$
Scalar–Jacobian chart	Azimuthal chart $T: \mathbb{R}^n \to M$ with log–Jacobian depending only on $ x $, i.e. $\log \det DT(x) = \psi(x)$
Lambert lift T_{ρ}	Equal-area (Lambert) chart L_p composed with a radial profile $\rho:[0,R_{\max})\to [0,\rho_*)$, see (3)
Radial Compensation (RC)	Choice of tangent–space base so that after any scalar–Jacobian chart, the manifold density is geodesic–radial and the Fisher information in radial parameters matches the 1D Euclidean Fisher
Balanced polar pushforward	RC generalised to arbitrary (M, g) via the polar volume factor J_p , see Theorem 3
Fisher–flat radial manifold	Parameter space in which the Fisher metric for radial parameters is the same as in Euclidean 1D and is independent of curvature and chart

Proofs

Let (M,g) be either $\mathbb{S}^n_{R_c}$ or \mathbb{H}^n_{-1/R_c^2} with pole $p \in M$. Let R(q) := d(p,q) be the geodesic radius and let $\operatorname{Exp}_p: T_pM \to M$ denote the Riemannian exponential map.

In polar coordinates $q=\mathrm{Exp}_p(R\Omega)$ with $\Omega\in\mathbb{S}^{n-1}$, the Riemannian volume element has the form

$$d\mathrm{vol}_M(q) = s_{\kappa}(R)^{n-1} dR d\Omega$$

for constant curvature κ , and more generally

$$d\mathrm{vol}_M(q) = J_p(R,\Omega) dR d\Omega$$

with polar volume factor $J_p(R,\Omega)$.

A scalar–Jacobian azimuthal chart $T: \mathbb{R}^n \to M$ about p satisfies

$$\log |\det DT(x)| = \psi(||x||) =: \log J_T(r), \qquad r = ||x||.$$

In polar Euclidean coordinates x=ru with $u\in\mathbb{S}^{n-1}$ we write T(x)=T(ru)=:q and R=d(p,q). On constant curvature spaces, the scalar–Jacobian identity is

$$J_T(r) = \left(\frac{s_{\kappa}(R(r))}{r}\right)^{n-1} R'(r).$$

Proof sketch of Theorem 1. Fix a scalar–Jacobian chart T with radial Jacobian factor $J_T(r)$. The RC base in the chart is

$$f_{\theta}(x) = \frac{1}{Z_{\theta}} \varphi_{\theta}(r) J_T(r), \qquad r = ||x||.$$

Write the pushforward density under T as

$$\rho_{\theta}(q) = f_{\theta}(T^{-1}q) \mid \det DT^{-1}(q) \mid.$$

Let x = ru and q = T(x); by definition of J_T ,

$$\left| \det DT^{-1}(q) \right| = \frac{1}{J_T(r)}.$$

Therefore

$$\rho_{\theta}(q) = \frac{1}{Z_{\theta}} \, \varphi_{\theta}(r) \, J_T(r) \, \frac{1}{J_T(r)} = \frac{1}{Z_{\theta}} \, \varphi_{\theta}(r).$$

Because T is azimuthal and scalar–Jacobian, the geodesic radius R(q) is a deterministic function of r only: $R = R_T(r)$. By construction of RC, the radial profile φ_θ has been chosen so that

$$\varphi_{\theta}(r) = \phi_{\theta}(R_T(r)).$$

Reparametrising by R, we obtain the geodesic-radial form

$$\rho_{\theta}(q) = \phi_{\theta}(R), \qquad R = d(p, q).$$

For the Fisher information, differentiate the log-likelihood:

$$\partial_{\theta} \log \rho_{\theta}(q) = \partial_{\theta} \log \phi_{\theta}(R).$$

There is no contribution from J_T because it cancels out in the pushforward, and the angular variable Ω is independent of θ under RC. Thus

$$I_M(\theta) = \mathbb{E}_{\theta} [(\partial_{\theta} \log \rho_{\theta}(Q))^2] = \mathbb{E}_{\theta} [(\partial_{\theta} \log \phi_{\theta}(R))^2] = I_R^1(\theta),$$

the Fisher information of the one-dimensional radial family $R \sim \phi_{\theta}$.

Finally, for the KL divergence between two RC models we have

$$\mathrm{KL}(\rho_{\theta} \parallel \rho_{\eta}) = \iint \phi_{\theta}(R) \, \log \frac{\phi_{\theta}(R)}{\phi_{\eta}(R)} \, J_{p}(R, \Omega) \, dR \, d\Omega.$$

Integrating over Ω produces the standard radial base measure S(R)dR (the area of the geodesic sphere of radius R), so

$$\mathrm{KL}(\rho_{\theta} \parallel \rho_{\eta}) = \int \phi_{\theta}(R) \, \log \frac{\phi_{\theta}(R)}{\phi_{\eta}(R)} \, S(R) \, dR = \mathrm{KL}(\phi_{\theta} \parallel \phi_{\eta}),$$

where the right-hand side is the one-dimensional KL with respect to the same base measure S(R)dR.

Dominated convergence and the usual regularity conditions ensure that differentiation under the integral is valid and the one–dimensional Fisher and KL are finite. This gives the claimed likelihood, Fisher, and KL invariances. \Box

This says that after RC the manifold model only sees a point through its geodesic radius R = d(p,q), and the statistics of the radial parameters are exactly the same as in the 1D Euclidean model ϕ_{θ} , including Fisher information and KL.

Proof sketch of Theorem 2. Let T_1 and T_2 be two scalar–Jacobian azimuthal charts about the same pole p, both equipped with RC bases built from the same radial family $\{\phi_{\theta}\}$. By Theorem 1, the pushforward under T_i satisfies

$$\rho_{\theta}^{(T_i)}(q) = \phi_{\theta}(R(q)), \qquad R(q) = d(p, q), \ i = 1, 2.$$

The right-hand side depends only on the manifold point q, not on the chart. Hence $\rho_{\theta}^{(T_1)} = \rho_{\theta}^{(T_2)}$ as densities on M.

The Fisher information for θ is

$$I_M^{(T_i)}(\theta) = \mathbb{E}\left[(\partial_{\theta} \log \rho_{\theta}^{(T_i)}(Q))^2 \right] = \mathbb{E}\left[(\partial_{\theta} \log \phi_{\theta}(R))^2 \right] = I_R^1(\theta),$$

again independent of the chart. Thus both likelihoods and Fisher information coincide across all scalar—Jacobian charts, completing the proof. \Box

This means that once you use RC, swapping one scalar–Jacobian chart for another (e.g. Exp to bExp or GCL) does not change either the geodesic–radial density or the Fisher information in the radial parameters: these charts differ only as numerical preconditioners.

Proof sketch of Theorem 3. Fix a pole p and write polar coordinates $q = \operatorname{Exp}_p(R\Omega)$ with $R \geq 0$, $\Omega \in \mathbb{S}^{n-1}$. The polar volume element is

$$d\mathrm{vol}_M(q) = J_p(R,\Omega) dR d\Omega.$$

Define the balanced base in $T_pM \cong \mathbb{R}^n$ by

$$f_{\theta}(x) = \frac{1}{Z_{\theta}} \phi_{\theta}(R) J_{p}(R, \Omega),$$

where x corresponds to the pair (R,Ω) under the polar map via the exponential chart. Here $J_p(R,\Omega)$ is exactly the Jacobian of the map $(R,\Omega) \mapsto q$ with respect to Lebesgue measure in (R,Ω) .

Now push forward to M. Let $Q = \text{Exp}_n(R\Omega)$ with density

$$\rho_{\theta}(q) = f_{\theta}(x) \mid \det D(\operatorname{Exp}_{p}^{-1})(q) \mid.$$

By construction, the Jacobian factor $J_p(R,\Omega)$ in $f_{\theta}(x)$ cancels with the inverse Jacobian $|\det D(\operatorname{Exp}_p^{-1})(q)| = 1/J_p(R,\Omega)$, yielding

$$\rho_{\theta}(q) = \frac{1}{Z_{\theta}} \, \phi_{\theta}(R).$$

Hence the pushforward is geodesic-radial with radial law ϕ_{θ} .

For the Fisher information, the log-likelihood is

$$\log \rho_{\theta}(q) = \log \phi_{\theta}(R) - \log Z_{\theta},$$

so the score in θ depends only on R. Therefore

$$I_M(\theta) = \mathbb{E}_{\theta} [(\partial_{\theta} \log \phi_{\theta}(R))^2] = I_R^1(\theta)$$

whenever the polar factor J_p is radial (e.g. constant curvature). In the general case, perturbations of J_p in R introduce only curvature—controlled error terms; a Taylor expansion of $\log J_p$ in R up to third order gives the bound claimed in the theorem.

Thus the balanced polar base produces geodesic–radial laws on any manifold with known polar volume element and preserves the one–dimensional radial Fisher information up to curvature-controlled error. \Box

This extends RC beyond spheres and hyperbolic spaces: on any manifold where we know the geodesic polar volume element J_p , multiplying a 1D radial law by J_p in polar coordinates yields a geodesic-radial model whose radius statistics are as close as possible to the Euclidean ones.

Proof sketch of Theorem 4. Let T be a scalar–Jacobian azimuthal chart with radial Jacobian factor $J_T(r)$, and consider isotropic bases

$$f_{\theta}(x) = h_{\theta}(r), \qquad r = ||x||.$$

Step 1 (Geodesic-radial form fixes h_{θ} up to J_T). Assumption (1) says that there exists a family $\{\varphi_{\theta}\}$ such that the pushforward density

$$\rho_{\theta}(q) = f_{\theta}(T^{-1}q) \mid \det DT^{-1}(q) \mid = \varphi_{\theta}(R(q)).$$

Let x = ru, q = T(x), and denote $R = R_T(r)$. Using $|\det DT^{-1}(q)| = 1/J_T(r)$, we get

$$\varphi_{\theta}(R_T(r)) = h_{\theta}(r) \frac{1}{J_T(r)}.$$

Since R_T is strictly increasing in r, we can rewrite this as

$$h_{\theta}(r) = \varphi_{\theta}(R_T(r)) J_T(r).$$

Thus any isotropic base satisfying (1) must be of the form "radial profile composed with R_T times J_T ". Step 2 (Fisher condition forces φ_{θ} to be the same 1D radial family as in (2)). Assumption (2) requires that

$$I_M(\theta) = I_R^1(\theta)$$

for the same radial family $\{\varphi_{\theta}\}$. But the Fisher on M computed from $h_{\theta}(r)$ is

$$I_M(\theta) = \mathbb{E}_{\theta} \left[(\partial_{\theta} \log h_{\theta}(r))^2 \right] - \text{(chart terms)}.$$

Using the relation $h_{\theta}(r) = \varphi_{\theta}(R_T(r))J_T(r)$ and the scalar–Jacobian identity, the chart terms coming from J_T and from the change of variable $r \mapsto R$ cancel exactly if and only if $h_{\theta}(r)$ has the RC form

$$h_{\theta}(r) \propto \varphi_{\theta}(r) J_T(r)$$

up to a smooth reparametrisation of θ . Any deviation would change the Fisher information away from the one–dimensional radial value.

Thus assumptions (1)–(2) force h_{θ} to coincide with the RC base (5) up to reparametrisation of θ , proving the claimed uniqueness.

Informally, this is the uniqueness result: within isotropic bases and scalar–Jacobian charts, RC is essentially the only way to have both geodesic–radial likelihoods and Euclidean–style Fisher information in the radial parameters. Any other choice must distort either the likelihood semantics or the Fisher geometry.

Proof sketch of Corollary 1. In constant curvature, the polar volume depends only on R, so Theorem 3 gives exact equality $I_M(\theta) = I_R^1(\theta)$ for any RC construction. By Theorems 1 and 2 we know that:

- 1. For any scalar–Jacobian chart T, the RC pushforward is $\rho_{\theta}(q) = \phi_{\theta}(d(p,q))$.
- 2. The Fisher information in θ equals the one–dimensional radial Fisher and is independent of T and of the curvature parameter κ .

Thus RC yields radial semantics that are invariant across both chart choices and curvature: the meaning of θ in terms of the radial law ϕ_{θ} is identical in all these settings.

Conversely, if an isotropic scalar–Jacobian model satisfies these properties, Theorem 4 applies and forces the base to be of RC form, up to reparametrisation. This establishes the "unique realisation" claim. \Box

Proof sketch of Corollary 2. Sufficiency. If we choose an RC base in any scalar–Jacobian chart T, Theorems 1 and 2 imply that the pushforward is geodesic–radial $\rho_{\theta}^{(T)}(q) = \phi_{\theta}(d(p,q))$ and that the Fisher in θ equals the one–dimensional Euclidean radial Fisher, independent of T. Hence learning θ is Fisher–equivalent to fitting a one–dimensional Euclidean radial model: RC is Fisher–efficient.

Necessity. Suppose instead that for some isotropic scalar–Jacobian model we have, for all charts T,

- geodesic-radial pushforwards with some radial family $\{\phi_{\theta}\}\$,
- Fisher information equal to the one–dimensional radial Fisher.

Fix a chart T and denote its base by $f_{\theta}(x) = h_{\theta}(||x||)$. The above two assumptions are exactly (1)–(2) in Theorem 4. By that theorem, h_{θ} must be of RC form

$$h_{\theta}(r) \propto \phi_{\theta}(r) J_T(r),$$

up to reparametrisation of θ . Since T was arbitrary, RC is necessary within this modelling class for Fisher-efficient radial learning, completing the proof.

So, within isotropic scalar–Jacobian models, RC is both sufficient and necessary for "Euclidean–style" radial learning: if your radial parameters behave like they do in 1D Euclidean space, you are implicitly using RC (up to reparametrisation).

Proof sketch (RC corollary: statistics). Under RC on a constant-curvature manifold, Theorem 1 gives

$$\rho_{\theta}(q) = \phi_{\theta}(R), \qquad R = d(p, q).$$

Therefore for any measurable function q,

$$\mathbb{E}_{\theta}[g(R)] = \int_{M} g(d(p,q)) \, \phi_{\theta}(d(p,q)) \, d\text{vol}_{M}(q).$$

Change variables to polar coordinates (R, Ω) , use $d\text{vol}_M(q) = s_{\kappa}(R)^{n-1} dR d\Omega$, and note that the angular term integrates to a constant absorbed into the normalisation of ϕ_{θ} . Thus the law of R is exactly ϕ_{θ} (on the appropriate support), and for any integer $m \geq 1$,

$$\mathbb{E}_{\theta}[R^m] = \int R^m \phi_{\theta}(R) \, dR,$$

with truncation of the integral on spheres to $R < \pi R_c$ as in the paper. Taking m = 1, 2 gives the "mean stays mean, variance stays variance" statements.

In other words, RC really does what it says on the tin: geodesic radii on the manifold have exactly the same one-dimensional moments as the target Euclidean radial law, up to the obvious truncation on spheres.

Proof sketch of Theorem 5. Assume the data come from an RC model with radial family $\{\phi_{\vartheta}\}$ and parameter ϑ^{\star} .

(i) The population negative log-likelihood satisfies

$$L(\theta) = \mathbb{E}_{\rho^*}[-\log \rho_{\theta}^{(T)}(Q)] = \mathrm{KL}(\rho^* \parallel \rho_{\theta}^{(T)}) + \mathrm{const.}$$

Any minimiser θ^* must satisfy $\rho_{\theta^*}^{(T)} = \rho^*$. Since $\rho^*(q) = \phi_{\vartheta^*}(d(p,q))$ is RC with Euclidean radial Fisher, Corollary 2 applies to the family $\{\rho_{\theta}^{(T)}\}$ and forces the corresponding tangent bases at θ^* to be of RC form.

(ii) If $\hat{\theta}_n$ is KL-consistent, then $\hat{\theta}_n \to \theta^*$ in probability and $\rho_{\hat{\theta}_n}^{(T)} \to \rho^*$. By the same argument as in (i), the limiting base at θ^* is RC, so the tangent bases learned by any such estimator converge to the RC base.

So if the truth is RC and your model class can express it, any KL-consistent learner will "discover" RC in the limit. RC is not just a convenient choice; it is the asymptotic attractor of likelihood matching within this class.

Proof sketch of Proposition 1. Let $T: \mathbb{R}^n \to M$ be an azimuthal chart about p with $\log |\det DT(x)| = \psi(||x||)$. Write x = ru and q = T(ru). Because T is azimuthal, it preserves directions: q lies along a geodesic in direction u', so T(ru) can be written as

$$T(ru) = \operatorname{Exp}_n(R(r)\Omega(u))$$

for some radial function R(r) and angular map $\Omega: \mathbb{S}^{n-1} \to \mathbb{S}^{n-1}$ that is independent of r.

In polar coordinates, the Lambert azimuthal equal–area map L_p has the form

$$L_p(\rho u) = \operatorname{Exp}_p(G(\rho) \Phi(u)),$$

where G is the Lambert radius profile and Φ is an angular isometry. Because T is azimuthal and scalar–Jacobian, its Jacobian determinant depends only on r. This forces the angular part to be measure– preserving on the sphere, so Ω is an isometry and can be absorbed into Φ . Thus T must factor through Lambert as

$$T(x) = L_p\left(\rho(\|x\|) \frac{x}{\|x\|}\right) =: T_\rho(x)$$

for some strictly increasing profile ρ with $\rho(0) = 0$.

Finally, comparing the Jacobian of T with that of L_p in polar coordinates yields exactly the scalar–Jacobian and radius identities stated in (4). Hence every scalar–Jacobian azimuthal chart is a Lambert lift for some profile ρ .

This says that every "nice" azimuthal chart you might use is just Lambert composed with some radial profile. Designing scalar–Jacobian charts is therefore equivalent to choosing a single scalar function $\rho(r)$.

Proof sketch of Theorem 6. The bExp profile ρ_{α} is defined as the solution of the ODE

$$\left(\frac{\rho_\alpha(r)}{r}\right)^{n-1}\rho_\alpha'(r) = \left(\frac{s_\kappa(r)}{r}\right)^{(n-1)\alpha}, \quad \rho_\alpha(0) = 0, \ \rho_\alpha'(0) = 1.$$

- 1. Existence and smoothness. This is a first-order ODE with smooth right-hand side for r > 0 and smooth initial conditions at r = 0. Standard ODE theory gives a unique C^{∞} solution on $[0, R_{\text{max}})$.
- 2. Strict monotonicity. The right-hand side is strictly positive for r > 0, so $\rho'_{\alpha}(r) > 0$ and ρ_{α} is strictly increasing.
- 3. Diffeomorphism property. Since ρ_{α} is strictly increasing with $\rho_{\alpha}(0) = 0$ and ρ'_{α} never vanishes, $r \mapsto \rho_{\alpha}(r)$ is a smooth diffeomorphism from a star domain onto its image. The azimuthal structure then implies that $T_{\alpha} := T_{\rho_{\alpha}}$ is a C^{∞} diffeomorphism from a star domain in \mathbb{R}^n onto its image in M; on \mathbb{H}^n it is global, while on \mathbb{S}^n it is global away from the cut locus $(r < R_{\text{max}})$.
- 4. Scalar log-det. Insert the ODE into the scalar-Jacobian identity (4):

$$\log|\det DT_{\alpha}(x)| = (n-1)\log\frac{\rho_{\alpha}(r)}{r} + \log\rho'_{\alpha}(r).$$

Using the ODE gives

$$\log |\det DT_{\alpha}(x)| = (n-1)\alpha \log \frac{s_{\kappa}(r)}{r},$$

i.e. a scalar function of r only, as claimed.

This says that $bExp_{\alpha}$ is always a smooth change of coordinates: for any $\alpha \in [0,1]$ it gives a well-behaved chart whose log-Jacobian is just a scalar multiple of the exponential map's log-Jacobian.

Proof sketch of Proposition 2. Expand ρ_{α} near r=0 as

$$\rho_{\alpha}(r) = r(1 + ar^2 + O(r^4)).$$

Use the Taylor series $s_{\kappa}(r) = r - \kappa r^3/6 + O(r^5)$ and plug into the defining ODE

$$\left(\frac{\rho_{\alpha}(r)}{r}\right)^{n-1}\rho_{\alpha}'(r) = \left(\frac{s_{\kappa}(r)}{r}\right)^{(n-1)\alpha}.$$

Match coefficients of r^2 to solve for a and obtain the local series expansion claimed in the proposition, including how the geodesic radius $d(p, bExp_{\alpha}(ru))$ deviates from r.

Differentiating the ODE in α gives a linear ODE for $\dot{\rho} = \partial_{\alpha} \rho_{\alpha}$ with right-hand side proportional to $\log(s_{\kappa}(r)/r)$. A comparison principle then shows that $|d(p, bExp_{\alpha}(ru)) - r|$ is nonincreasing in α and vanishes as $\alpha \to 1$, establishing the monotonicity in α .

Proof sketch of Theorem 7. Consider the functional

$$E_{\alpha}[\rho] = \int_{0}^{R^{*}} r^{n-1} \left\{ \frac{1}{n} (1 - \alpha) \left[(n-1) \log(\rho(r)/r) + \log \rho'(r) \right]^{2} + \alpha \left[G(\rho(r)) - r \right]^{2} \right\} dr$$

on the class C of smooth strictly increasing profiles with $\rho(0) = 0$, $\rho'(0) = 1$, where $G(\rho) = 2 \operatorname{ars}(\rho/2)$.

- 1. Strict convexity. Set $v = \log(\rho/r)$, $y = \log \rho'$. Then the "volume" term is a positive quadratic form in (v, y), hence strictly convex. The "geodesic" term is a strictly convex functional of ρ because $G'(\rho) \ge 1$ and the integrand is a squared deviation.
- 2. Euler-Lagrange equation. Compute the first variation of $E_{\alpha}[\rho]$. The Euler-Lagrange equation for a critical point reduces (after algebra and using the polar factor identities) to the ODE

$$\left(\frac{\rho(r)}{r}\right)^{n-1}\rho'(r) = \left(\frac{s_{\kappa}(r)}{r}\right)^{(n-1)\alpha},$$

which is precisely (6)–(7), i.e. the defining equation for ρ_{α} .

3. Uniqueness. Since E_{α} is strictly convex on C and ρ_{α} satisfies the Euler-Lagrange equation, it must be the unique minimiser of E_{α} in C.

The Pareto-optimality statement follows from viewing E_{α} as a convex combination of a "volume error" and a "geodesic error": moving along α traces the Pareto frontier between those two objectives.

Informally, this shows that $bExp_{\alpha}$ is not an ad-hoc interpolation: it is the unique solution to a clean optimisation problem that trades off volume distortion against geodesic error, and the dial α parametrises the lower Pareto frontier of this trade-off.

Proof sketch of Theorem 8. Define the GCL chart by taking $\Phi(r) = 2s_{\kappa}(r/2)$ and

$$\mathcal{G}(x) := L_p(\Phi(\|x\|) x / \|x\|), \qquad r = \|x\|.$$

By Proposition 1, any scalar–Jacobian azimuthal chart can be written as a Lambert–lift $T_{\rho}(x) = L_{p}(\rho(r) x/||x||)$ for some strictly increasing profile ρ . For such a T_{ρ} , the polar identities (4) give

$$R_{\rho}(r) = d(p, T_{\rho}(ru)) = 2 \operatorname{ars}\left(\frac{\rho(r)}{2}\right), \qquad \log|\det DT_{\rho}(ru)| = (n-1)\log\frac{\rho(r)}{r} + \log\rho'(r),$$

where ars is arcsin on the sphere and arsinh in hyperbolic space.

For \mathcal{G} we choose $\rho = \Phi$. Using the inverse relation $\operatorname{ars}(s_{\kappa}(t)) = t$ we obtain

$$d(p, \mathcal{G}(ru)) = 2 \operatorname{ars}\left(\frac{\Phi(r)}{2}\right) = 2 \operatorname{ars}\left(s_{\kappa}(r/2)\right) = r = ||x||,$$

so GCL is geodesic-exact: $d(p, \mathcal{G}(x)) = ||x||$.

Differentiating $\Phi(r) = 2s_{\kappa}(r/2)$ gives $\Phi'(r) = c_{\kappa}(r/2)$. Plugging $\rho = \Phi$ and $\rho' = \Phi'$ into the scalar–Jacobian identity yields

$$\log|\det D\mathcal{G}(x)| = (n-1)\log \frac{\Phi(r)}{r} + \log \Phi'(r) = (n-1)\log \frac{s_{\kappa}(r/2)}{r/2} + \log c_{\kappa}(r/2),$$

the claimed scalar log-determinant.

For uniqueness, let T_{ρ} be any Lambert–lift with scalar radial Jacobian that is geodesic–preserving: $d(p, T_{\rho}(ru)) = r$ for all r. By the radius identity above this means

$$2 \operatorname{ars}\left(\frac{\rho(r)}{2}\right) = r \quad \Rightarrow \quad \rho(r) = 2 \, s_{\kappa}(r/2) = \Phi(r),$$

since $G(\rho) = 2 \operatorname{ars}(\rho/2)$ is strictly increasing and hence invertible. Thus $\rho = \Phi$ and $T_{\rho} = \mathcal{G}$, i.e. any geodesic–preserving Lambert–lift with scalar radial Jacobian coincides with GCL.

So GCL is the "geodesically correct" Lambert-lift: it keeps geodesic radii exact while still having a scalar log-Jacobian, and within the Lambert-lift class it is the unique chart with those two properties.

Proof sketch of Proposition 3. Consider $bExp_{\alpha}$ or GCL in polar coordinates. The differential in the splitting (radial, angular) has singular values controlled by:

- the radial factor $\rho'(r)$ (or $\Phi'(r)$ for GCL),
- the angular scaling $\rho(r)/r$ (or $\Phi(r)/r$).

On a compact shell $A_{\delta,R} := \{x : \delta \leq ||x|| \leq R\}$ both $\rho(r)/r$ and $\rho'(r)$ are bounded away from 0 and ∞ by smoothness and monotonicity; likewise for Φ . Hence the operator norm ||DT(x)|| is bounded above and below by positive constants L_{α}, m_{α} on $A_{\delta,R}$.

Applying the mean–value inequality along line segments in \mathbb{R}^n gives

$$m_{\alpha}||x-y|| \le d(T(x),T(y)) \le L_{\alpha}||x-y||$$

for all x, y in the shell, i.e. bExp $_{\alpha}$ and GCL are bi–Lipschitz on compact shells with the claimed constants. \Box

This says that on any fixed annulus in the tangent space, $bExp_{\alpha}$ and GCL distort distances only by bounded factors. They behave like well-conditioned linear preconditioners rather than wild warps.

Proof sketch of Proposition 4. For the "no free lunch" part, work in the Lambert-lift class. By Proposition 1 any scalar–Jacobian azimuthal chart has the form $T_{\rho}(x) = L_{p}(\rho(r)x/||x||)$ with radial profile $\rho(r)$. The Jacobian determinant is

$$\log|\det DT_{\rho}(x)| = (n-1)\log\frac{\rho(r)}{r} + \log\rho'(r).$$

If T_{ρ} is volume–preserving, this log–det is identically zero. If T_{ρ} is geodesic–preserving, the geodesic radius is $R(r) = 2 \operatorname{ars}(\rho(r)/2)$. Near r = 0, geodesic preservation forces $R(r) = r + O(r^3)$, hence $\rho(r) = 2s_{\kappa}(r/2) = r - \kappa r^3/24 + O(r^5)$. Plugging this expansion into the Jacobian identity shows that, unless $\kappa = 0$, the coefficient of r^2 in $\log |\det DT_{\rho}|$ is nonzero, so the chart cannot be volume–preserving. Thus for $\kappa \neq 0$ no azimuthal chart can be simultaneously unit–volume and geodesic–preserving.

For the blow–up on $\mathbb{S}^n_{R_c}$, consider any geodesic–preserving Lambert–lift, and in particular GCL. From Theorem 8,

$$\log |\det D\mathcal{G}(x)| = (n-1) \log \frac{s_{\kappa}(r/2)}{r/2} + \log c_{\kappa}(r/2), \qquad r = ||x||.$$

On the sphere $s_{\kappa}(r/2) = R_c \sin(r/2R_c)$ stays bounded and nonzero as $r \uparrow \pi R_c$, while $c_{\kappa}(r/2) = R_c \cos(r/2R_c) \to 0$. A Taylor expansion about $r = \pi R_c$ gives

$$c_{\kappa}(r/2) \approx C(\pi R_c - r), \qquad \log c_{\kappa}(r/2) \approx \log(\pi R_c - r) + \text{const},$$

so the radial derivative behaves like

$$\left|\partial_r \log |\det D\mathcal{G}(x)|\right| \asymp \frac{1}{\pi R_c - r}$$
 as $r \uparrow \pi R_c$.

Since ∇_x points roughly in the radial direction, this implies

$$\|\nabla_x \log|\det DT(x)|\| \gtrsim \frac{c}{\pi R_c - r}$$

for some c > 0 and r close to πR_c . This is the claimed near-cut-locus blow-up for any geodesic-preserving azimuthal chart on the sphere.

So there really is no perfect chart on a curved manifold: you cannot have both exact geodesics and perfectly flat volume, and any geodesic-preserving chart must become badly conditioned near its cut locus. This is why we resort to atlases and smooth gating there.

Proof sketch of Theorem 9. On $\mathbb{S}^n_{R_c}$ take two antipodal scalar–Jacobian azimuthal charts T_+ and T_- centred at p and -p. Each chart has a cut locus at the opposite pole. Choose a smooth partition of unity $\psi_+, \psi_- : \mathbb{S}^n_{R_c} \to [0,1]$ such that $\psi_+ + \psi_- = 1$ everywhere, and ψ_+ vanishes in a small neighbourhood of the cut locus of T_+ (and similarly for ψ_-).

Let $\ell_{\pm}(q)$ be the per–sample log–likelihood expressed in chart T_{\pm} (i.e. the Euclidean backbone plus the chart log–det). Away from their cut loci, T_{\pm} are smooth diffeomorphisms with bounded Jacobian and inverse Jacobian, and the backbone is C^1 (or C^2), so each ℓ_{\pm} is C^1 (resp. C^2) with bounded derivatives on compacta in its domain. Define the global log–likelihood by gating:

$$\ell(q) := \psi_{+}(q) \,\ell_{+}(q) + \psi_{-}(q) \,\ell_{-}(q).$$

Near the cut locus of T_+ , the gate ψ_+ vanishes, so ℓ agrees with the smooth function $\psi_-(q)\ell_-(q)$ there, and conversely near the cut locus of T_- . On the overlap region where both charts are valid, ψ_\pm and ℓ_\pm are smooth, and ℓ is just a finite linear combination of smooth functions with smooth coefficients, hence C^1 (and C^2 if the backbone is). Because we stay a fixed distance $\delta > 0$ away from both cut loci on the supports of ψ_\pm , all chart derivatives and Jacobians are uniformly bounded in those regions, so $\nabla \ell$ (and $\nabla^2 \ell$ when they exist) are uniformly bounded on compact sets.

This proves that the two–chart atlas with a smooth gate yields a global per–sample log–likelihood that is C^1 (and often C^2) with bounded first and second derivatives.

This guarantees that when we cover the sphere with two antipodal charts and a smooth gate, the resulting log-likelihood is globally smooth with bounded gradients, so optimisation does not see any artificial kinks at the seams.

Proof sketch of Theorem 10. For an RC model under a scalar–Jacobian chart $T_{\alpha} = b \text{Exp}_{\alpha}$, the per–sample log–likelihood decomposes into

$$\log \rho_{\theta}(q) = \log \phi_{\theta}(R) + \log |\det DT_{\alpha}^{-1}(q)|.$$

The first term does not depend on α ; the second is the "chart term".

By Theorem 6,

$$\log |\det DT_{\alpha}(x)| = (n-1)\alpha \log \frac{s_{\kappa}(r)}{r}.$$

Inverting the chart shows that the chart term is

$$\log|\det DT_{\alpha}^{-1}(Q)| = -(n-1)\alpha\log\frac{s_{\kappa}(R)}{R},$$

where R = d(p, Q) is the geodesic radius under RC. Hence

$$\operatorname{Var}\left[\log|\det DT_{\alpha}^{-1}(Q)|\right] = \alpha^{2}\operatorname{Var}\left[(n-1)\log\frac{s_{\kappa}(R)}{R}\right],$$

which is the claimed α^2 scaling.

For the gradient bound, write the full gradient as $\nabla_{\theta}\ell_{\alpha} = \nabla_{\theta}\ell_{\text{backbone}} + \nabla_{\theta}\ell_{\text{chart}}$. Under RC the dependence of R on θ is controlled by the 1D radial Fisher $I_R^1(\theta)$, and the backbone gradient is L_{θ} -Lipschitz on a compact shell. Combining this with the variance bound on the scalar chart term and the fact that the atlas gate is C^1 with bounded derivatives gives

$$\operatorname{Var}[\nabla_{\theta} \ell_{\alpha}] \leq C_1 \alpha^2 \operatorname{Var}\left[(n-1) \log \frac{s_{\kappa}(R)}{R}\right] + C_2(L_{\theta}, \delta),$$

for constants C_1, C_2 independent of α , as stated.

This quantifies the benefit of the bExp dial: under RC, the variance coming from the chart term scales like α^2 , so moving away from $\alpha = 1$ (the raw exponential) can dramatically reduce gradient and Hutchinson variance without changing the underlying likelihood.

Proof sketch of Theorem 11. For a CNF on \mathbb{H}^d written in an RC chart T_{α} , the ODE for the latent variable x_t has a vector field whose divergence contains the chart term $\nabla_x \log |\det DT_{\alpha}(x)|$.

From the scalar log-det formula in Theorem 6,

$$\log|\det DT_{\alpha}(x)| = (n-1)\alpha\log\frac{s_{-1}(r)}{r},$$

and differentiation gives

$$\|\nabla_x \log |\det DT_{\alpha}(x)|\| \lesssim \alpha |r \partial_r \log (s_{-1}(r)/r)|.$$

On \mathbb{H}^d , $s_{-1}(r) \sim \frac{1}{2}e^r$ for large r, so the right-hand side grows linearly with r but with a prefactor α . RC ensures that the distribution of geodesic radii remains matched to ϕ_{θ} , so typical radii stay in a moderate range and the stiffness induced by the chart term scales at most linearly with α , rather than exploding with curvature.

Bounding the Lipschitz constant of the CNF vector field in terms of this gradient yields the stated upper bound on stiffness (and hence on the number of function evaluations) with explicit dependence on α .

This connects the chart choice to CNF cost: smaller α makes the chart term less stiff, so adaptive ODE solvers can take larger steps and need roughly $1/\alpha$ fewer NFEs for the same tolerance, again without changing the realised density under RC.

Proof sketch of Theorem 12. On \mathbb{H}^d in the hyperboloid model, the geodesic radius R and ambient norm ||x|| are related roughly by

$$R \approx \operatorname{arcosh}\left(1 + \|x\|^2/2\right).$$

Curvature proxies used in practice (e.g. ambient norms, projected distances) deviate from true R with errors that grow with curvature and radius.

Under RC, the radial law ϕ_{θ} controls the distribution of R, and the bExp/GCL charts keep the radius mapping close to the identity or with controlled distortion. This implies that perturbations in the curvature proxy (e.g. using ||x|| instead of R) translate into bounded perturbations of the likelihood and its gradients.

A sensitivity calculation, differentiating the log–likelihood with respect to the proxy and using the RC moment identities, yields the explicit bounds in the theorem, showing that RC suppresses curvature– induced sensitivity in a controlled way.

Intuitively: once RC has "cleaned up" the radial law, moderate errors in the curvature proxy (or even the curvature value itself) only have a mild, controlled effect on gradients. This matches the empirical observation that mixed-curvature VAEs can be surprisingly robust to small curvature mismatch.

Additional empirical details and ablations

We present implementation details, additional diagnostics, and extended experiments that complement the main text. We keep the notation and theorem numbering from the main paper.

Synthetic RC verification

Implementation details. For the synthetic experiments on \mathbb{S}^2 and \mathbb{H}^2 we fix the pole as p=(0,0,1) on the sphere and the origin in the hyperboloid model for hyperbolic space. On \mathbb{S}^2 we draw radii from $R \sim \text{TruncNormal}(\mu=1.0, \sigma=0.35)$ on $[0, \pi)$; on \mathbb{H}^2 from $R \sim \text{HalfNormal}(\sigma=0.5)$. Directions are always $\Omega \sim \text{Unif}(S^1)$ and samples are formed as $q = \exp_p(R\Omega)$. For each chart we draw $N = 2 \cdot 10^4$ samples per seed for 5 seeds.

Geodesic radii are computed exactly from the ambient coordinates. We estimate empirical means and variances of R and evaluate the radius $\mathrm{KL}(\widehat{p}(R) \parallel \phi_{\theta}(R))$ on a fixed radial grid (500 points on $[0, \pi)$ for \mathbb{S}^2 and [0, 5] for \mathbb{H}^2) using numerical quadrature.

Additional radial families. On \mathbb{H}^2 we also test RC bases that realise Gamma, Weibull, and Lognormal radial laws, again with $\Omega \sim \mathrm{Unif}(S^1)$. For each family we vary shape/scale parameters to cover both light and heavy tails. In all cases RC charts (Exp, bExp, GCL) recover the intended geodesic radial laws up to sampling noise, while Exp (raw) induces effective shape and scale parameters that deviate substantially from the target values. These results provide additional empirical support for the RC invariance statements in Theorems 1–2.

Gaussian base experiment. For E1b we fix a Euclidean base $X \sim \mathcal{N}(0, 0.25I_2)$ in T_pM and push it through \exp_p with and without RC. Table 3 shows that the RC-Exp base again produces geodesic radial laws that match the target TruncNormal / HalfNormal families on \mathbb{S}^2 and \mathbb{H}^2 , whereas Exp (raw) yields biased means, variances, and significantly larger radius KLs, in line with the polar-factor analysis in Sec. 3.

Mixed-Curvature VAE details and extensions

Architecture and training. For the Mixed-Curvature VAE we follow Skopek et al. [18]. The latent manifold is

$$M_0 = \mathbb{S}_{K_{\mathrm{S}}}^{n_{\mathrm{S}}} \times \mathbb{H}_{K_{\mathrm{H}}}^{n_{\mathrm{H}}} \times \mathbb{R}^{n_{\mathrm{E}}}$$

with $(n_{\rm S}, n_{\rm H}, n_{\rm E})$ chosen so that the total latent dimension matches the Euclidean baseline. The encoder and decoder are shallow convolutional networks; we use Adam with a fixed learning rate and train for 10 epochs on MNIST.

The baseline prior uses wrapped Gaussians implemented via the raw exponential map on each constant–curvature factor. The RC–bExp prior uses the same radial families but replaces each non–flat factor by an RC base with a scalar–Jacobian chart (Exp or bExp $_{\alpha}$). Curvatures $K_{\rm S}$, $K_{\rm H}$ are initialised near ± 1 and learned jointly with the rest of the parameters.

Extended diagnostics. Figure 8 (right) shows curvature trajectories for both methods. Under the wrapped-Exp baseline, the spherical curvature drifts from $K_{\rm S}\approx 1.0$ to $K_{\rm S}\approx 2.5$, while the hyperbolic factor flattens from $K_{\rm H}\approx -0.95$ to $K_{\rm H}\approx -0.48$, consistent with curvature being partly absorbed by chart distortions. Under RC-bExp, the spherical component is driven close to flat $(K_{\rm S}\approx 0.14)$ and the hyperbolic component sharpens to $K_{\rm H}\approx -1.62$, while the Euclidean factor remains numerically flat $(K_{\rm E}\approx 0)$. Across multiple seeds we observe qualitatively similar curvature trajectories and ELBO gaps.

Reconstruction NLL curves for the two methods almost coincide, while the KL term is consistently smaller under RC-bExp throughout training, as anticipated by the curvature mis-specification analysis in

Theorem 12. Decoder traversals on a 2D slice of the Euclidean latent block (Fig. 9) show that RC-bExp produces more class-consistent and smoothly varying grids than the wrapped-Exp baseline, supporting the interpretation that RC improves local latent geometry without changing the architecture.

Additional datasets. On Fashion–MNIST, using the same $S \times H \times \mathbb{R}$ latent geometry, we observe the same qualitative behaviour: RC–bExp improves ELBO relative to the wrapped–Exp baseline at nearly unchanged reconstruction NLL, and the curvature trajectories remain stable. We omit detailed tables for brevity.

Hyperspherical VAE details

Model and optimisation. The \mathbb{S}^{16} VAE in Sec. 5.3 uses a small convolutional encoder with ReLU nonlinearities and a fully connected layer that outputs mean and (log) variance in $T_p\mathbb{S}^{16}$. The decoder is a mirrored convnet with Bernoulli likelihood. We use a single global pole p, standard reparameterisation in the tangent space, and push samples to \mathbb{S}^{16} using either Exp (raw) or RC–Exp. All optimisation hyperparameters (Adam, learning rate, and schedule) are shared across charts.

Posterior radii. Posterior geodesic radii R = d(p,q) for Exp (raw) and RC-Exp are shown in Fig. 10. In both cases the empirical radii concentrate in a narrow band, but RC-Exp yields radii that are slightly better aligned with the HalfNormal prior of scale $\sigma = 0.5$, reflected in a lower radius KL (Table 6). These results complement the larger ELBO gains of the mixed-curvature experiment in Sec. 5.2, and are consistent with the Fisher-equivalence guarantees for RC in Theorems 1–2.

Latent CNFs: additional ablations

Solver and logging. For all latent CNF experiments we use a Dormand-Prince 5(4) ODE solver with absolute and relative tolerances shared across charts on a given dataset. We log the number of function evaluations (NFEs), the scalar chart term $\log |\det DT_{\alpha}^{-1}(Q)|$, and its contribution to the gradient variance. The NFEs and chart-term variances reported in Table 7 and Fig. 11 are averaged over test batches at the final epoch.

Variance and CNF stiffness vs. α . In addition to the chart–term variance reported in the main text, we track the empirical variance of the gradient of the chart term with respect to θ . On all four image datasets we observe the same qualitative scaling as for the chart term itself: $\operatorname{Var}[\nabla_{\theta} \log | \det DT_{\alpha}^{-1}|]$ decreases approximately quadratically in α , consistent with Theorem 10. The total gradient variance (including the CNF state) also decreases with α , but more weakly, reflecting that the chart term is only one contribution to the overall variance.

Stability across seeds and learning rates. For the high–dimensional CIFAR–10 setting we repeat the $d_z=64$ experiments across multiple seeds and learning rates. With Exp (raw), a substantial fraction of runs exhibit the catastrophic blow–ups described in Sec. 5.4: mean radii grow to very large values and test NLL spikes. In contrast, RC–Exp and RC–bExp_{0.5} remain stable under the same learning rates and solver tolerances; geodesic radii stay in a moderate range and NLL remains well behaved. These observations further support the CNF stiffness bounds in Theorem 11.

Hyperbolic flows on WordNet

Dataset and model. We use the WordNet mammals subgraph with the same preprocessing as in prior hyperbolic-flow work. Nodes are embedded into \mathbb{H}^d using a coupling–flow architecture with a latent CNF component and a fixed pole p. All flows share the same coupling layers and CNF backbone; only the chart (Exp vs. RC–Exp vs. RC–bExp_{0.5} vs. RC–GCL) and the tangent base (standard vs. RC) are changed.

Additional diagnostics. Beyond the main metrics in Table 8, we inspect the distribution of geodesic radii and the coverage of hyperbolic balls. RC charts align empirical radii more closely with the intended radial prior, whereas Exp (raw) shows mild curvature–induced distortions. However, all charts achieve similar link–prediction performance and geodesic calibration, indicating that in this regime the primary effect of RC is on parameter semantics and numerical conditioning rather than on the task loss itself.

Protein orientations on \mathbb{S}^3 (\mathbf{E}_{prot})

Data construction. We extract central–residue frames from PDB entries 1CRN, 1UBQ, 2PTC, and 4HHB using a standard pipeline (backbone atoms, local alignment, quaternion normalisation). Each example consists of a 26-dimensional local context and a unit quaternion $q \in \mathbb{S}^3$ defining the target orientation.

Model details. The conditional backbone is a small MLP that outputs the parameters of a tangent–space Gaussian at a fixed pole p. We map to \mathbb{S}^3 using either Exp (raw), RC–Exp, or RC–bExp_{0.5} and evaluate a wrapped Gaussian likelihood. Training uses Adam with the same learning rate, batch size, and early stopping criterion across charts.

Extended results. Table 9 in the main text shows that RC–Exp and RC–bExp_{0.5} reduce test NLL from 2.60 to ≈ 0.9 nats compared to Exp (raw), while leaving the geodesic frame error essentially unchanged. The small difference between RC–Exp and RC–bExp_{0.5} is consistent with the RC invariance results for scalar–Jacobian charts: once the radial law is specified in geodesic units, changing α mainly affects Jacobian bookkeeping and numerical conditioning.

RC priors for hyperbolic graph embeddings

Objective and setup. We test whether RC priors can make hyperbolic graph embeddings more geometrically faithful and curvature–stable than the standard wrapped–Exponential construction, without degrading link–prediction quality. We consider two graphs with hierarchical structure: (i) the WordNet mammals subgraph; and (ii) a synthetic balanced tree with added cross–links. Nodes are embedded into \mathbb{H}^d_{-1/R_c^2} (hyperboloid model) with a fixed pole p. Each node v has a Euclidean parameter $x_v \in T_pM$ mapped to $q_v = T(x_v) \in M$ by a chart T. We train with a margin–based loss on geodesic distances, plus a radial prior term on node radii $R_v = d(p, q_v)$ with a 1D law ϕ_θ (HalfNormal or Gamma).

We compare: (i) Exp (raw) with an isotropic Gaussian base in T_pM ; (ii) RC–Exp with an RC base realising $R_v \sim \phi_\theta$; and (iii) RC–bExp with bExp $_\alpha$ charts and the same RC base. Hyperparameters and training budgets are shared across conditions.

Results. On the synthetic tree, RC priors yield higher or comparable AUC and MRR than Exp (raw) for curvature radii $R_c \in \{0.5, 1.0, 2.0\}$, while substantially improving alignment between node radius and graph depth and reducing the radius–prior KL. Within the RC family, smaller α values in bExp charts reduce the variance of the radial–prior gradient approximately as α^2 (Theorem 10), again without hurting link–prediction quality. On WordNet mammals the trends are qualitatively similar but noisier: RC priors improve curvature stability and radial calibration while keeping AUC and MRR comparable to, or slightly better than, Exp (raw). These experiments illustrate that RC priors can enforce meaningful geodesic radii in graph embeddings while preserving, and sometimes improving, downstream performance.

RC priors for feature geometry in classifiers

Objective and setup. Beyond generative modelling, we use RC to control feature geometry in classifiers. We train small convolutional classifiers on MNIST and CIFAR-10 whose penultimate layer lives on a sphere or a hyperbolic space. The network maps an input x to a tangent feature vector $v(x) \in T_pM \cong \mathbb{R}^d$ and then to a manifold feature $z(x) = T(v(x)) \in M$, with $M \in \{\mathbb{S}^d, \mathbb{H}^d\}$ and scalar–Jacobian chart T. Class logits are

negative squared geodesic distances to per-class prototypes $\{c_k\}$,

$$\ell_k(x) = -\frac{1}{\tau} d_M(z(x), c_k)^2,$$

followed by a softmax.

We consider two ways of regularising feature radii R(x) = d(p, z(x)): (i) Exp (raw) with a standard ℓ_2 penalty on ||v(x)||; and (ii) an RC prior in which the target geodesic-radius law $R \sim \phi_{\theta}$ (HalfNormal with $\sigma_R = 1$) is enforced via a one-dimensional moment-matching penalty between the empirical radius distribution and ϕ_{θ} .

Metrics and results. Table 11 reports test accuracy, NLL, expected calibration error (ECE), and a radius KL between the empirical distribution of R(x) and the HalfNormal prior. On MNIST, the RC prior keeps accuracy and NLL close to the Exp (raw) baseline while reducing radius KL, i.e., geodesic feature radii adhere more closely to the intended prior. On CIFAR-10, RC priors yield stable geodesic radii across spherical and hyperbolic heads, with correctly classified examples concentrating at larger radii than misclassified ones, consistent with geodesic radius acting as a margin-like quantity. This illustrates an additional non-generative use case for RC: it provides a principled way to shape feature geometry without modifying the classifier backbone.

Dataset / manifold	Prior	Acc (%) ↑	NLL ↓	ECE ↓	radius KL \downarrow
MNIST, \mathbb{S}^{16}	Exp (raw)	99.35	0.456	0.354	1.85
MNIST, \mathbb{S}^{16}	RC	98.59	0.491	0.363	1.61
CIFAR-10, \mathbb{S}^{16}	RC	77.57	0.992	0.311	0.27
CIFAR-10, \mathbb{H}^{16}	RC	74.44	0.763	0.037	0.27

Table 11: RC feature priors (last epoch). Test accuracy, NLL, calibration (ECE) and one–dimensional radius KL between empirical feature radii R(x) = d(p, z(x)) and a HalfNormal prior with $\sigma_R = 1$. On MNIST, the RC prior keeps predictive performance close to the Exp (raw) baseline while pulling geodesic radii closer to the intended prior. On CIFAR–10, RC yields stable geodesic radii across spherical and hyperbolic heads, with correctly classified examples concentrating at larger radii than misclassified ones (mean radius ≈ 1.22 vs. 0.74 on the sphere).

Baseline without RC. For completeness, we also trained a spherical classifier with Exp (raw) and a HalfNormal radius prior implemented only via an ℓ_2 penalty on tangent features. The model achieves $\approx 98\%$ test accuracy on MNIST with test cross–entropy around 1.15 nats but exhibits poor calibration (ECE ≈ 0.66). Geodesic radii still correlate with softmax margins, confirming the geometric picture in which features organise along a geodesic "margin band"; RC makes this prior explicit and curvature-/chart-invariant.

S0. Measure–theoretic foundations for RC

Lemma 1 (Absolute continuity and differentiation under the integral). Let T be a scalar–Jacobian azimuthal chart about p with radial Jacobian factor $J_T(r)$ and let $\{\varphi_{\theta}\}$ be a dominated family on $[0, R_{\text{max}})$. Define

$$f_{\theta}^{\text{base}}(x) \propto \varphi_{\theta}(\|x\|) J_T(\|x\|) \qquad (x \in \mathbb{R}^n).$$

Then the pushforward of f_{θ}^{base} through T is absolutely continuous w.r.t. dvol_M, and ∂_{θ} can be interchanged with the integral in the log-likelihood and in the Fisher information whenever $\partial_{\theta} \log \varphi_{\theta}$ admits an integrable envelope.

Proof. Work in geodesic polar coordinates around p, where $d\text{vol}_M = s_{\kappa}(R)^{n-1} dR d\omega$ with R = d(p,q). The scalar–Jacobian assumption implies that in these coordinates the Jacobian of T depends only on r = ||x||, so the pushforward measure admits a density by the coarea formula. Dominated convergence applies to $\partial_{\theta} \log \varphi_{\theta}$ under the envelope assumption, yielding differentiation under the integral sign in both likelihood and Fisher.

S1. Radial calculus and Lambert-lift Jacobian

Throughout, write x = ru with r = ||x|| and $u \in \mathbb{S}^{n-1}$. For any radial function g(x) = h(r),

$$\nabla g(x) = h'(r) u,$$

$$\nabla^2 g(x) = h''(r) u u^{\top} + \frac{h'(r)}{r} (I - u u^{\top}).$$

Let L_p be an azimuthal Lambert chart at p (equal-area, so $|\det DL_p| \equiv 1$ on its domain), and let $\rho: [0, R_{\text{max}}) \to [0, \rho_*)$ be a strictly increasing smooth radial profile with $\rho(0) = 0$. Define the Lambert-lift

$$T_{\rho}(x) = L_{p}\left(\rho(\|x\|) \frac{x}{\|x\|}\right), \qquad T_{\rho}(0) := p.$$

Then in polar coordinates x = ru one has

$$\log\left|\det DT_{\rho}(x)\right| = (n-1)\log\frac{\rho(r)}{r} + \log\rho'(r), \qquad d\left(p, T_{\rho}(ru)\right) = 2 \operatorname{ars}\left(\frac{\rho(r)}{2}\right), \tag{8}$$

where

$$s_{\kappa}(r) = \begin{cases} \sin r, & \kappa = +1, \\ \sinh r, & \kappa = -1, \end{cases} \quad c_{\kappa}(r) = \begin{cases} \cos r, & \kappa = +1, \\ \cosh r, & \kappa = -1, \end{cases} \quad \operatorname{ars}(z) = \begin{cases} \arcsin z, & \kappa = +1, \\ \operatorname{arsinh} z, & \kappa = -1. \end{cases}$$

S2. Scalar-Jacobian azimuthal charts

Proposition 5 (Representation of scalar–Jacobian azimuthal charts). Let $M \in \{\mathbb{S}^n, \mathbb{H}^n\}$ and $p \in M$. Let $T : \mathbb{R}^n \to M$ be a smooth azimuthal chart about p, i.e. $T(ru) = \Gamma(r)u'$ where u' is the image of $u \in \mathbb{S}^{n-1}$ under an isometry of the tangent sphere. Assume $\log |\det DT(x)| = \psi(||x||)$ depends only on r = ||x||. Then there exists a strictly increasing C^{∞} profile ρ with $\rho(0) = 0$ such that

$$T(x) = L_p(\rho(||x||) \frac{x}{||x||}) =: T_\rho(x),$$

and the Jacobian and radius relations are given by (8).

Proof. Azimuthality implies $T(ru) = \Gamma(r)u'$ for some scalar $\Gamma(r)$ and some isometry $u \mapsto u'$. The scalar–Jacobian condition forces the area scaling to be radial. The equal–area property of L_p shows that every such T can be written as $L_p \circ \tilde{T}$ with $\tilde{T}(x) = \rho(||x||)x/||x||$ for some radial ρ . Composition of polar Jacobians yields (8).

S3. Balanced–Exponential (bExp) chart

Definition. Fix $\alpha \in [0,1]$ and $\kappa \in \{+1,-1\}$. Let $\rho_{\alpha} : [0,R_{\max}) \to [0,2)$ be the unique C^{∞} solution of

$$\left(\frac{\rho_{\alpha}(r)}{r}\right)^{n-1}\rho_{\alpha}'(r) = \left(\frac{s_{\kappa}(r)}{r}\right)^{(n-1)\alpha}, \qquad \rho_{\alpha}(0) = 0, \quad \rho_{\alpha}'(0) = 1. \tag{9}$$

Define, for $x \neq 0$ with r = ||x|| and u = x/||x||,

$$\operatorname{bExp}_{\alpha}(x) := L_{p}(\rho_{\alpha}(r) u), \quad \operatorname{bExp}_{\alpha}(0) := p.$$

Proposition 6 (Integral representation). For each $\alpha \in [0,1]$ the solution of (9) admits the integral form

$$\rho_{\alpha}(r) = \left[n \int_0^r t^{(n-1)(1-\alpha)} s_{\kappa}(t)^{(n-1)\alpha} dt \right]^{1/n}.$$

Proof. Rewrite (9) as

$$\rho_{\alpha}^{n-1}\rho_{\alpha}' = r^{(n-1)(1-\alpha)}s_{\kappa}(r)^{(n-1)\alpha}$$

Integrating and using $\rho_{\alpha}(0) = 0$ gives $\rho_{\alpha}(r)^n = n \int_0^r t^{(n-1)(1-\alpha)} s_{\kappa}(t)^{(n-1)\alpha} dt$. Taking *n*-th roots yields the claimed formula. Strict positivity of the integrand ensures ρ_{α} is strictly increasing.

Theorem 13 (Diffeomorphism and scalar log-det). For every $\alpha \in [0, 1]$, bExp_{\alpha} is a C^{∞} diffeomorphism from a star-shaped neighbourhood of $0 \in \mathbb{R}^n$ onto $M \setminus \{-p\}$. Moreover,

$$\left|\det D \operatorname{bExp}_{\alpha}(x)\right| = \left(\frac{s_{\kappa}(\|x\|)}{\|x\|}\right)^{(n-1)\alpha}.$$
(10)

In particular, $\alpha = 0$ recovers Lambert ($|\det| \equiv 1$) and $\alpha = 1$ reproduces the radial log-determinant of the exponential map.

Proof. Equation (9) has a unique C^{∞} solution with $\rho'_{\alpha} > 0$ by standard ODE theory, so ρ_{α} is strictly increasing. Combining (8) with (9) gives

$$\log \left| \det D \operatorname{bExp}_{\alpha}(x) \right| = (n-1) \log \frac{\rho_{\alpha}(r)}{r} + \log \rho_{\alpha}'(r) = (n-1)\alpha \log \frac{s_{\kappa}(r)}{r},$$

yielding (10). Strict monotonicity in r and smoothness imply that $bExp_{\alpha}$ is a local diffeomorphism away from 0, and the azimuthal structure gives a global diffeomorphism onto M minus the antipode.

Proposition 7 (Local expansion and monotonicity in α). As $r \downarrow 0$,

$$\rho_{\alpha}(r) = r \left(1 - \frac{(n-1)\alpha \kappa}{6(n+2)} r^2 + O(r^4) \right), \qquad d(p, b \operatorname{Exp}_{\alpha}(ru)) = r + O(\kappa r^3).$$

Moreover, for each fixed r in the domain, the geodesic mismatch $|d(p, bExp_{\alpha}(ru)) - r|$ is nonincreasing in α and vanishes as $\alpha \uparrow 1$.

Proof. Write $\rho_{\alpha}(r) = r(1 + ar^2 + O(r^4))$. Using $s_{\kappa}(r) = r - \kappa r^3/6 + O(r^5)$ in (9) and matching r^2 coefficients yields $a = -(n-1)\alpha\kappa/(6(n+2))$. For the geodesic radius, use $ars(z) = z + \kappa z^3/6 + O(z^5)$ at $z = \rho_{\alpha}(r)/2$ together with (8).

Differentiating (9) with respect to α gives a linear ODE for $\dot{\rho} = \partial_{\alpha}\rho_{\alpha}$ whose right-hand side has the sign of $\log(s_{\kappa}(r)/r)$. A comparison argument shows that $|\rho_{\alpha}(r) - \rho_{1}(r)|$ and hence $|d(p, bExp_{\alpha}(ru)) - r|$ is nonincreasing in α .

Theorem 14 (Variational optimality). Let C be the class of smooth, strictly increasing $\rho: [0, R_*] \to [0, 2)$ with $\rho(0) = 0$, $\rho'(0) = 1$. For $\alpha \in [0, 1]$ define

$$\mathcal{E}_{\alpha}[\rho] = \int_{0}^{R_*} r^{n-1} \left\{ (1-\alpha) \left[(n-1) \log \frac{\rho(r)}{r} + \log \rho'(r) \right]^2 + \alpha \left(2 \operatorname{ars} \left(\frac{\rho(r)}{2} \right) - r \right)^2 \right\} dr.$$

Then ρ_{α} from (9) is the unique minimiser of \mathcal{E}_{α} in \mathcal{C} .

Proof. Set $v = \log(\rho/r)$ and $y = \log \rho'$. The volume term is

$$D_{\text{vol}}(\rho) = \int r^{n-1} ((n-1)v + y)^2 dr,$$

which is strictly convex in (v, y). The geodesic term is

$$D_{\text{geo}}(\rho) = \int r^{n-1} (G(\rho) - r)^2 dr, \quad G(\rho) = 2 \operatorname{ars}(\rho/2),$$

and $G'(\rho) \ge 1$, so D_{geo} is strictly convex in ρ . The Euler–Lagrange equation for $(1 - \alpha)D_{\text{vol}} + \alpha D_{\text{geo}}$ reduces to (9), hence its unique solution ρ_{α} minimises \mathcal{E}_{α} .

Proposition 8 (Bi–Lipschitz bounds on shells). Let $A_{\delta,R} := \{x : \delta \leq ||x|| \leq R < R_{\max}\}$. There exist positive constants m_{α}, L_{α} , depending on $\inf_{A_{\delta,R}} \rho'_{\alpha}$ and $\sup_{A_{\delta,R}} \rho'_{\alpha}$, such that

$$m_{\alpha}||x-y|| \le d(\text{bExp}_{\alpha}(x), \text{bExp}_{\alpha}(y)) \le L_{\alpha}||x-y|| \qquad (x, y \in A_{\delta, R}).$$

Proof. The differential of bExp $_{\alpha}$ in polar coordinates is diagonal in the radial/angular splitting with singular values controlled by $\rho'_{\alpha}(r)$ and $\rho_{\alpha}(r)/r$. On $A_{\delta,R}$ these are bounded away from 0 and ∞ , giving operator–norm bounds on $DbExp_{\alpha}$ and hence, by the mean value inequality, bi–Lipschitz bounds.

S4. Geodesic-Corrected Lambert (GCL)

Theorem 15 (Geodesic preservation and scalar log-det). Let $\Phi(r) := 2 s_{\kappa}(r/2)$ and define

$$GCL(x) := L_p\Big(\Phi(\|x\|) \, \frac{x}{\|x\|}\Big).$$

Then

$$d(p, GCL(x)) = ||x||, \qquad \log \left| \det D GCL(x) \right| = (n-1) \log \frac{s_{\kappa}(r/2)}{r/2} + \log c_{\kappa}(r/2),$$

with r = ||x||.

Proof. Using (8) with $\rho(r) = \Phi(r) = 2s_{\kappa}(r/2)$ yields

$$d(p, GCL(ru)) = 2 \operatorname{ars}(s_{\kappa}(r/2)) = r,$$

and the stated log-det expression follows directly.

Proposition 9 (Incompatibility of unit volume and exact geodesics; blow-up near cut locus). If $\kappa \neq 0$, no azimuthal chart can be both volume-preserving ($|\det DT| \equiv 1$) and geodesic-preserving. Moreover, for any geodesic-preserving chart on \mathbb{S}^n (e.g. GCL),

$$\|\nabla_x \log|\det DT(x)|\| \sim \frac{c}{\pi - R}$$
 as $R \uparrow \pi$,

with R = d(p, T(x)).

Proof. Geodesic preservation within the Lambert–lift class forces $\rho(r) = 2s_{\kappa}(r/2)$. Substituting into (8) and expanding at r = 0 gives

$$\det DT_{\rho} = \left(\frac{2s_{\kappa}(r/2)}{r}\right)^{n-1} c_{\kappa}(r/2) = 1 + \kappa \frac{n+2}{24}r^2 + O(r^4) \neq 1$$

whenever $\kappa \neq 0$, so unit volume and geodesic preservation are incompatible. On \mathbb{S}^n one has $c_{\kappa}(r/2) = \cos(r/2) \to 0$ as $r \uparrow \pi$, and differentiation shows $\nabla_x \log |\det DT|$ diverges like $1/(\pi - R)$.

S5. Atlas regularity on \mathbb{S}^n

Theorem 16 (Two-chart atlas with smooth gate). Let \mathbb{S}^n be equipped with two azimuthal charts centred at antipodal poles p and -p. Fix $\delta > 0$ and choose a C^{∞} partition of unity $\{\psi_+, \psi_-\}$ such that the support of ψ_+ stays at distance $> \delta$ from the cut locus of p and similarly for ψ_- . Define

$$\log p(q) = \psi_{+}(q) \log p_{+}(q) + \psi_{-}(q) \log p_{-}(q).$$

where p_{\pm} are the chart-wise densities. Then the per-sample log-likelihood is C^1 on \mathbb{S}^n (and C^2 when the Euclidean backbone is C^2), and its gradient and Hessian are bounded on compact sets.

Proof. Away from the cut loci each chart is smooth and scalar–Jacobian, so $\log p_{\pm}$ inherit the regularity of the Euclidean backbone. Cross–terms appear only through $\nabla \psi_{\pm}$ and $\nabla^2 \psi_{\pm}$, which are bounded by construction on the supports. Combining the two charts with the gate and applying the chain rule yields C^1/C^2 regularity and uniform bounds on compacta.

S6. Variance bounds and CNF complexity

Let Q be distributed under some RC model on M and let R = d(p, Q).

Theorem 17 (Chart–term variance). For the inverse bExp chart,

$$\log \left| \det D \operatorname{bExp}_{\alpha}^{-1}(Q) \right| = \alpha(n-1) \log \frac{s_{\kappa}(R)}{R},$$

and hence

$$\operatorname{Var} \left[\log \left| \det D \operatorname{bExp}_{\alpha}^{-1}(Q) \right| \right] = \alpha^2 \operatorname{Var} \left[(n-1) \log \frac{s_{\kappa}(R)}{R} \right].$$

Proof. The inverse–chart identity follows by inverting (10). Variance scales quadratically with the multiplicative factor α .

Theorem 18 (CNF stiffness and NFEs). Let $\chi_{\alpha}(q)$ denote the instantaneous change-of-variables term of a coordinate CNF whose chart contribution is that of bExp $_{\alpha}$. On any compact set K away from the cut locus,

$$\operatorname{Lip}(\chi_{\alpha}; K) \leq \alpha \operatorname{Lip}(\chi_1; K),$$

where χ_1 is the corresponding term for $\alpha = 1$ (exponential chart). Consequently, for any adaptive p-th order Runge-Kutta method with scalar tolerance, the step size on K is bounded below by c/α and

$$\mathbb{E}[NFE_{\alpha}] \leq a + \frac{b}{\alpha}$$

for dataset- and solver-dependent constants a, b.

Proof. On \mathbb{S}^n one has $\nabla_x \log |\det D \exp_p(x)| = (n-1)(\cot r - 1/r)u$, and the bExp analogue is multiplied by α . A similar expression holds on \mathbb{H}^n with coth and csch. Differentiating and taking suprema over K yields the Lipschitz bound. Embedded RK error control chooses steps inversely proportional to the Lipschitz modulus, so step sizes scale like $1/\alpha$ and NFEs like $1/\alpha$ up to additive constants.

S7. RC on product manifolds and wrapped CNFs

Proposition 10 (RC on products of constant–curvature spaces). Let

$$M_0 = \prod_{i=1}^k M_{K_i}^{n_i}, \qquad M_{K_i}^{n_i} \in \{\mathbb{S}_{K_i}^{n_i}, \mathbb{H}_{K_i}^{n_i}, \mathbb{R}^{n_i}\},$$

with pole $p_0 = (p_1, \ldots, p_k)$. For each factor choose a scalar–Jacobian azimuthal chart $T_i : \mathbb{R}^{n_i} \to M_{K_i}^{n_i}$ about p_i with radial Jacobian factor $J_{T_i}(r_i)$ and a target one–dimensional radial density $\varphi_{\theta,i}$ on $[0, R_{\max,i})$. Define the RC base on $\prod_i T_{p_i} M_{K_i}^{n_i} \cong \mathbb{R}^{\sum_i n_i}$ in product polar coordinates by

$$p_{\text{base}}(r_1, \omega_1, \dots, r_k, \omega_k) \propto \prod_{i=1}^k \varphi_{\theta,i}(r_i) J_{T_i}(r_i),$$

with independent $\omega_i \sim \text{Unif}(\mathbb{S}^{n_i-1})$, and let $T = (T_1, \dots, T_k)$. If Q = T(X) denotes the pushforward on M_0 , then:

- 1. $R_i = d(p_i, Q_i)$ are independent and satisfy $R_i \sim \varphi_{\theta,i}$ for all i;
- 2. the Fisher information decomposes as

$$I_{M_0}(\theta) = \sum_{i=1}^k I_{R_i}(\theta),$$

where I_{R_i} is the one-dimensional Fisher information of $\varphi_{\theta,i}$.

Proof. Product polar coordinates give a product splitting of the volume form, and each factor behaves as in the one–dimensional RC construction. Independence and the Fisher decomposition follow from Fubini's theorem and additivity of log–likelihoods.

Corollary 3 (Variance reduction for wrapped CNFs). Consider coordinate CNFs on \mathbb{S}^n or \mathbb{H}^n built with either the exponential chart \exp_p or its balanced-exponential counterpart $\operatorname{bExp}_{\alpha}$, using the same neural vector field and Hutchinson trace estimator. On any compact shell away from the cut locus, the contribution of the chart term to the variance of the log-density estimate under $\operatorname{bExp}_{\alpha}$ is at most α^2 times the corresponding variance under \exp_p .

Proof. Let $\chi_{\alpha}(R)$ denote the scalar chart term in the inverse log–det. From (10) one has $\chi_{\alpha}(R) = \alpha \chi_1(R)$, so $\operatorname{Var}[\chi_{\alpha}(Q)] = \alpha^2 \operatorname{Var}[\chi_1(Q)]$. The Hutchinson estimator is linear in χ_{α} , hence its variance inherits the same factor.

S8. Curvature mis-specification and distributional proximity

Theorem 19 (Sensitivity to curvature proxies). Let κ be the true curvature and let the chart use a proxy $\tilde{\kappa} \neq \kappa$ in its Jacobian factor $s_{\tilde{\kappa}}$. Under an RC construction with the same radial base φ_{θ} , the difference between the per-sample θ -gradients of the log-likelihoods under κ and $\tilde{\kappa}$ satisfies, on any radius shell $R \leq R_0$,

$$\left\| \nabla_{\theta} \ell_{\alpha}^{(\tilde{\kappa})} - \nabla_{\theta} \ell_{\alpha}^{(\kappa)} \right\| \leq \alpha (n-1) L \sup_{r \leq R_0} \left| \Delta'(r) \right|, \qquad \Delta(r) := \log \frac{s_{\tilde{\kappa}}(r)}{s_{\kappa}(r)},$$

where L is a Lipschitz constant of the backbone network on the shell. For $r \ll 1$ one has $\sup_{r \leq R_0} |\Delta'(r)| \leq C R_0$ for a constant C depending on $\kappa, \tilde{\kappa}$.

Proof. Under RC, the only κ -dependent term in the θ -gradient is the scalar chart correction proportional to $\log(s_{\kappa}(r)/r)$. Replacing κ by $\tilde{\kappa}$ changes this term by $\alpha(n-1)\Delta'(R)$ inside the chain rule. Lipschitz continuity of the backbone w.r.t. its input yields the stated bound. A Taylor expansion of s_{κ} near 0 gives the small-r behaviour of $\Delta'(r)$.

Proposition 11 (Wasserstein proximity to \exp_p). Let $Q_{\alpha} = (b \operatorname{Exp}_{\alpha})_{\#} P$ and $Q_1 = (\exp_p)_{\#} P$ with $\operatorname{supp}(P) \subset \{x : \|x\| \leq R_0\}$. Then

$$W_2(Q_{\alpha}, Q_1) \leq C(n, \kappa, R_0) (1 - \alpha) R_0^2 \sqrt{\mathbb{E}[\|X\|^2]}.$$

Proof. Use the pointwise bound on the geodesic mismatch between bExp_{α} and exp_{p} on the support of P, which is $O((1-\alpha)r^2)$ from the local expansion and monotonicity in α . Integrate this bound in L^2 to obtain the Wasserstein estimate.

S9. RC examples and wrapped normals

Corollary 4 (RC upgrade of wrapped normal priors). Let $M \in \{\mathbb{S}^n_K, \mathbb{H}^n_K\}$ with curvature κ and pole $p \in M$. Consider the wrapped normal family obtained by pushing forward $v \sim \mathcal{N}(0, \Sigma)$ through $\exp_p : z = \exp_p(v)$. In geodesic polar coordinates (R, Ω) around p, its log-density can be written

$$\log p_{\mathrm{WN}}(z) = \log \mathcal{N}(v; 0, \Sigma) - (n-1) \log \frac{s_{\kappa}(R)}{R}, \qquad R = d(p, z).$$

Define instead the RC base

$$p_{\text{base}}^{\text{RC}}(v) \propto \mathcal{N}(v; 0, \Sigma) \left(\frac{s_{\kappa}(\|v\|)}{\|v\|}\right)^{n-1}.$$

Then the induced manifold density p^{RC} satisfies

$$\log p^{\text{RC}}(z) = \log \mathcal{N}(v; 0, \Sigma) + C(\kappa, n),$$

for a constant $C(\kappa, n)$ independent of Σ and z. In particular, the geodesic radius R = d(p, z) has the same marginal law as ||v|| in Euclidean space, and the Fisher information in Σ coincides with its Euclidean value.

Common radial families under RC. Let R = d(p, Q) be the geodesic radius.

- Gaussian-type. On \mathbb{S}^n , R has a truncated Normal law on $[0,\pi)$; on \mathbb{H}^n , R can be HalfNormal or shifted Normal on $[0,\infty)$. Geodesic moments coincide with the corresponding one-dimensional formulas (with truncation on \mathbb{S}^n).
- Gamma / Weibull. On \mathbb{H}^n , choosing $R \sim \text{Gamma}(k,\beta)$ yields $\mathbb{E}[R] = k\beta$ and $\text{Var}[R] = k\beta^2$; on \mathbb{S}^n the law truncates to $[0,\pi)$.
- Lognormal / folded-t. Heavy-tailed choices such as folded-t (with degrees of freedom ν) carry their moment properties to geodesic radius, truncated as needed on \mathbb{S}^n .

Cauchy specialization. Taking the folded-t with $\nu = 1$ gives a Cauchy law on the radius.

• On \mathbb{H}^n , R is half-Cauchy with scale s > 0:

$$\varphi_{\mathrm{HC}}(R;s) = \frac{2}{\pi s} \frac{1}{1 + (R/s)^2}, \qquad R \in [0, \infty).$$

• On \mathbb{S}^n , R is a truncated half-Cauchy on $[0,\pi)$:

$$\varphi_{\mathrm{HC},S}(R;s) = \frac{1}{Z_S(s)} \frac{2}{\pi s} \frac{1}{1 + (R/s)^2} \mathbf{1}_{[0,\pi)}(R), \qquad Z_S(s) = \frac{2}{\pi} \arctan \frac{\pi}{s}.$$

All moments are finite; for instance

$$\mathbb{E}[R] = \frac{s}{2\arctan(\pi/s)}\ln\left(1 + \frac{\pi^2}{\mathbb{S}^2}\right), \qquad \mathbb{E}[R^2] = \frac{\pi s}{\arctan(\pi/s)} - \mathbb{S}^2,$$

and $Var[R] = \mathbb{E}[R^2] - \mathbb{E}[R]^2$. These follow by direct integration, and RC ensures they hold for the geodesic radius on \mathbb{S}^n .

Isotropy and sampling. RC models are isotropic about p: sample $R \sim \varphi_{\theta}$ on $[0, R_{\text{max}})$, $\Omega \sim \text{Unif}(\mathbb{S}^{n-1})$, set $X = R\Omega \in T_pM$, and output Q = T(X). Then d(p, Q) = R and $\rho_{\theta}(q) = \varphi_{\theta}(d(p, q))$.

S10. Volume–preserving charts on Thurston geometries

We record volume-preserving base charts on the eight Thurston model geometries and their bExp-lifts.

Theorem 20 (Lambert charts for Thurston geometries). Each Thurston model geometry \mathcal{G} admits an explicit C^{∞} chart $L: \mathbb{R}^3 \to \mathcal{G}$ with $\det \nabla L \equiv 1$ relative to the Riemannian volume on \mathcal{G} .

Proof sketch. On \mathbb{S}^3 and \mathbb{H}^3 take the azimuthal Lambert map L_p at a pole with $\rho(r) \equiv r$ in (8), which yields $|\det DL_p| \equiv 1$. Products of model spaces inherit volume preservation from the factors by multiplicativity of the Jacobian. On the Lie–group geometries (NIL, Soll, \widetilde{SL}_2), work in standard left–invariant coordinates where Riemannian volume equals Haar measure and compose with a triangular shear/scaling of unit determinant to obtain L.

A convenient cho<u>ice of such charts is summarised in Table 12.</u>

Here $\lambda_{+1}(r) = \sqrt{1 - \frac{r^2}{4}}$ and $\lambda_{-1}(r) = \sqrt{1 + \frac{r^2}{4}}$, and $L_{\mathbb{S}^2}$, $L_{\mathbb{H}^2}$ denote the corresponding two–dimensional Lambert charts.

Given such an L and a radial profile ρ_{α} solving

$$\left(\frac{\rho_{\alpha}(r)}{r}\right)^2 \rho_{\alpha}'(r) = \mu_{\mathcal{G}}(r)^{\alpha}, \qquad \rho_{\alpha}(0) = 0, \ \rho_{\alpha}'(0) = 1,$$

for an appropriate direction-averaged radial factor $\mu_{\mathcal{G}}(r)$, define the bExp-lift on \mathcal{G} by

$$T_{\alpha}(x) = L\left(\rho_{\alpha}(\|x\|) \frac{x}{\|x\|}\right).$$

Then $\log |\det \nabla T_{\alpha}(x)| = \alpha \log \mu_{\mathcal{G}}(||x||)$ is scalar and radial, and the RC construction on \mathcal{G} proceeds exactly as in the constant–curvature case.

Table 12: Example volume–preserving charts $L:\mathbb{R}^3 \to \mathcal{G}$ with unit Jacobian.

Geometry	Coordinates	Volume–preserving chart L
\mathbb{E}^3	(x, y, z)	L(x, y, z) = (x, y, z)
\mathbb{S}^3 (azimuthal)	$x \in \mathbb{R}^3$	$L(x) = (\lambda_{+1}(r) x/r, -1 + \frac{1}{2}r^2), r = x $
\mathbb{H}^3 (hyperboloid)	$x \in \mathbb{R}^3$	$L(x) = (\lambda_{-1}(r) x/r, 1 + \frac{1}{2}r^2), r = x $
$\mathbb{S}^2 \times \mathbb{R}$	(x,t)	$L(x,t) = \left(L_{\mathbb{S}^2}(x), t\right)$
$\mathbb{H}^2 \times \mathbb{R}$	(x,t)	$L(x,t) = \left(L_{\mathbb{H}^2}(x), t\right)$
Nil (Heisenberg)	(x, y, z)	$L(x,y,z) = \left(x, \ y, \ z + \frac{1}{2}xy\right)$
Sol	(x, y, z)	$L(x, y, z) = (e^{z/2}x, e^{-z/2}y, z)$
$\widetilde{\mathrm{SL}}_2$ (Iwasawa)	(x, y, z)	$L(x, y, z) = (u, v, w) = (x, ye^{-2x}, z)$